Benchmark solutions

# High-order, stable, and conservative boundary schemes for central and compact finite differences

P.T. Brady*, D. Livescu

*CCS-2, Los Alamos National Laboratory, Los Alamos, NM 87545, USA*

A B S T R A C T

Stable and conservative numerical boundary schemes are constructed such that they do not diminish the overall accuracy of the method for interior schemes of orders 4, 6, and 8 using both explicit (central) and compact finite differences. Previous attempts to develop stable numerical boundary schemes for non-linear problems have resulted in schemes which significantly reduced the global accuracy and/or required some form of artificial dissipation. Thus, the schemes developed in this paper are the first to not require this tradeoff, while also ensuring discrete conservation and allowing for direct boundary condition enforcement. After outlining a general procedure for the construction of conservative boundary schemes of any order, a simple, yet novel, optimization strategy which focuses directly on the compressible Euler equations is presented. The result of this non-linear optimization process is a set of high-order, stable, and conservative numerical boundary schemes which demonstrate excellent stability and convergence properties on an array of linear and non-linear hyperbolic problems.

© 2019 Elsevier Ltd. All rights reserved.

## 1. Introduction

High fidelity simulations of flow problems (such as Direct Numerical Simulations) are usually performed more efficiently using high order methods. For example, conservative, high-order numerical methods are, in principle, well suited to the challenge of accurately resolving the broadband physics of turbulence over long periods of time. In practice, however, numerical stability is not easily achieved for high-order methods. In particular, when high order finite differences are used, the computational stencil used in the interior must be altered near the computational boundary for non-periodic domains.

Designing high-order numerical boundary schemes such that they are stable for non-linear problems is a very difficult task [1,2]. The most prevalent solution to this problem is to simply reduce the order of the boundary schemes by roughly half [3–8]. Indeed, this practice has become an accepted standard such that many researchers simply do not report the modifications made to the schemes near the boundaries. The problem with combining a high order interior scheme with a reduced order boundary stencil is that the overall order of accuracy will be limited to 1 more than the boundary stencils [9]. Thus, pursuing a high-order inte-

rior scheme while maintaining a significantly reduced order at the boundary is not particularly efficient.

The search for stable, high-order boundary schemes has a long history and is still an active field. Ref. [1] relied on the linear stability theory to frame the problem of finding stable schemes for linear hyperbolic problems and used an eigenvalue search code to find stable 4th order compact schemes as well explicit 5th order schemes for a 6th order compact interior scheme. In a follow-up work, Ref. [10] utilized the energy method to design stable compact boundary schemes for interior orders up to 6 through the development of the summation-by-parts simultaneous approximate term (SBP-SAT) method. This comes at the expense of imposing the boundary conditions weakly via a penalty term added to the equations. Schemes which allow for direct imposition of the boundary condtions have proved to be very useful for DNS and so the focus of the present work is on such methods.

A different approach, developed in Ref. [11], involves reducing the grid spacing near the boundaries to stabilize the numerical boundary schemes. The approach is based on the insight that the instabilities which typically develop when using one-sided differences near the boundary are simply a manifestation of the well known Runge phenomenon. The authors were able to generate schemes with appropriate eigenvalue spectra of up to 22nd order. As presented, the boundary schemes were not conservative. Such an approach would decrease the allowable timestep size for explicit numerical integration.

---

* Corresponding author.
  *E-mail address:* ptb@lanl.gov (P.T. Brady).

Another popular approach is to introduce a filtering operation to stabilize the numerical scheme [12–14]. The constraints imposed by high fidelity, DNS-type calculations, have motivated the search for an alternate approach targeting the construction of stable, high-order, and conservative numerical boundary schemes which do not require modifications of the grid near the boundaries, artificial dissipation, or weak enforcement of the boundary conditions. Rather than attempting to develop a general theory of stability for non-linear systems, the focus of this paper is on developing schemes which are stable for a particular system of interest: the non-linear equations of fluid dynamics. Conservative schemes of overall accuracy of orders 4, 6, and 8 (where the order of the numerical boundary schemes is one less) are developed for both explicit and compact finite differences. This is achieved through a simple, yet novel, optimization strategy where we optimize directly on the non-linear Euler equations rather than attempting to utilize a linear stability theory. The procedure relies on the introduction of enough free parameters in the boundary stencils such that the problem admits solutions. Note that the focus of the present work is on continuous solutions to the governing equations. The Euler equations are only used as a stringent, zero-dissipation test case, for times small enough so that singularities do not develop during the simulation.

The paper is organized as follows. The procedure for constructing high-order conservative schemes with an appropriate number of free parameters is outlined in Section 2. First, the interior spatial discretization for central and compact finite differences of order 4, 6, and 8, together with discrete conservation constraints are discussed. This is followed by the methodology of constructing conservative boundary schemes. The section concludes with the properties of the non-optimized base schemes, in which all the free parameters are set to zero. The purpose of examining this problem is to note that all non-optimized base schemes of order greater than 4 are unstable for the test problem, highlighting the need for some kind of optimization strategy that yields suitably stable schemes. The optimization strategy for the free parameters is discussed in Section 3. A variety of tests which demonstrate the stability of the optimized schemes for both linear and non-linear problems are presented in Section 4 and Section 5 contains the conclusions. The coefficients for the optimized boundary schemes are given in the Appendix.

## 2. Numerics

The primary target of the stable, conservative and high-order finite differences schemes developed here is high-fidelity, DNS-type, simulations of compressible flows. In general, the effects of the molecular transport terms (viscous stress tensor, diffusion, and thermal heat conduction) are dissipative in nature. As such, they can easily mask instabilities in a numerical method for certain flow regimes. To avoid this uncertainty and get a clearer picture of stability, the focus of the optimization procedure used here is on the compressible Euler equations for which conservation of mass, momentum and energy are given by:

$$\frac{\partial \rho}{\partial t} + \frac{\partial \rho u_i}{\partial x_i} = 0, \tag{1}$$

$$\frac{\partial \rho u_i}{\partial t} + \frac{\partial \rho u_i u_j}{\partial x_j} = -\frac{\partial p}{\partial x_i}, \tag{2}$$

$$\frac{\partial \rho E}{\partial t} + \frac{\partial \rho E u_i}{\partial x_i} = -\frac{\partial p u_i}{\partial x_i}, \tag{3}$$

where $\rho$ is the density, $p$ the pressure, $E$ the total energy, $u_i$ the $i$th component of the velocity vector, and the Einstein summation

**Table 1**
Coefficients for first derivative central (explicit) finite differences approximation of order $2p$ given by Eq. (6).

| $p$ | $\gamma_1$ | $\gamma_2$ | $\gamma_3$ | $\gamma_4$ |
|---|---|---|---|---|
| 2 | $\frac{2}{3}$ | $-\frac{1}{12}$ | | |
| 3 | $\frac{3}{4}$ | $-\frac{3}{20}$ | $\frac{1}{60}$ | |
| 4 | $\frac{4}{5}$ | $-\frac{1}{5}$ | $\frac{4}{105}$ | $-\frac{1}{280}$ |

convention is assumed. The system is then closed by an equation of state assuming a calorically perfect gas,

$$p = (\gamma - 1)(\rho E - \rho u_i u_i / 2). \tag{4}$$

The speed of sound, $a$, is given by

$$a = \sqrt{\gamma p / \rho}. \tag{5}$$

For the numerical tests, the ratio of specific heats, $\gamma$, is assumed equal to 1.4, corresponding to air.

The focus of the present work is on continuous (smooth) solutions to the governing equations. This is due to the goal of developing schemes suitable for DNS of compressible flows. The proper application of DNS is Navier–Stokes-type equations, where the existence of smooth solutions is guaranteed for smooth enough initial conditions. Here, the Euler equations are only used as a stringent, zero-dissipation test case, for times small enough so that singularities do not develop during the simulation.

The procedure for generating high-order conservative discretizations to this system is split into 4 subsections. The interior spatial discretization is discussed in Section 2.1. The constraints which a discretization must satisfy to be discretely conservative as well as a general procedure for constructing high-order conservative boundary schemes are discussed in Sections 2.2 and 2.3, respectively. The stability of non-optimized base schemes, with the free parameters set to zero, is discussed in Section 2.4 for a test problem.

### 2.1. Interior spatial discretization

In the interior of the domain, standard central and compact finite differences are used to approximate the spatial derivatives. For these schemes, a stencil of order $2(p + s)$ and centered at point $i$ on a grid with constant spacing $h$, has the form,

$$\sum_{k=-s}^{k=s} \delta_k f'_{i+k} = \frac{1}{h} \sum_{j=-p}^{j=p} \gamma_j f_{i+j} + \mathcal{O}\left(h^{2(p+s)}\right), \tag{6}$$

where $\gamma_{-j} = -\gamma_j$, $\delta_{-k} = \delta_k$, $\gamma_0 = 0$, $\delta_0 = 1$, and $f$ are the known function values used to approximate the derivative, $f'$. The coefficients $\delta_k$ and $\gamma_j$ are derived in a straightforward manner by matching the Taylor series coefficients for the left and right hand sides of Eq. (6). For further details of how this can be done systematically, the interested reader can see the discussions in Ref. [15,16]. Schemes with $s = 0$ correspond to explicit finite differences. These are shown in Table 1 for $p \in \{2, 3, 4\}$. Observe that schemes with $s > 0$ require the solution of a linear system to evaluate the derivative and are typically labeled according to the structure of this system. Thus, stencils with $s = 1$ correspond to tridiagonal schemes [15]. Coefficients for the combination of $(s, p)$ considered in this paper are listed in Table 2.

### 2.2. Discrete conservation constraints

In the ensuing discussion the following notations are adopted: (a) bold capital letters, $\boldsymbol{A}$, refer to matrices, (b) regular capital letters, $F$, refer to column vectors, (c) lowercase letters, $f$, refer to continuous functions, and (d) indexed lowercase letters, $u_i$, refer to a discrete value

**Table 2**
Coefficients for first derivative compact finite differences approximation of order $2(p + s)$ given by Eq. (6).

| $(s, p)$ | $\delta_1$ | $\gamma_1$ | $\gamma_2$ | $\gamma_3$ |
|----------|------------|------------|------------|------------|
| $(1, 1)$ | $\frac{1}{4}$ | $\frac{3}{4}$ | | |
| $(1, 2)$ | $\frac{1}{3}$ | $\frac{7}{9}$ | $\frac{1}{36}$ | |
| $(1, 3)$ | $\frac{3}{8}$ | $\frac{25}{32}$ | $\frac{1}{20}$ | $-\frac{1}{480}$ |

For hyperbolic systems, it is often advantageous to use conservative approximations as these ensure the computed solution maintains certain physical invariants. Conservation, in the Lax–Wendroff sense [17], ensures convergence to the correct discontinuous weak solutions. However, the focus of the present paper is on continuous solutions. Thus, we adopt a definition of conservation prevalent in the DNS community. The basis of the current approach can be found in Ref. [15] and is expanded upon below.

To define a "conservative" approximation, consider a scalar hyperbolic conservation law with the form:

$$\frac{\partial u}{\partial t} + \frac{\partial f}{\partial x} = 0, \tag{7}$$

for $x \in [0, L]$ where $f = f(u)$ is some flux function. The solution to this equation has the property that the total change of $u$ as a function of time is driven solely by the flux function, $f$, at the domain boundaries. This can be seen by integrating Eq. (7) over the domain:

$$\frac{d}{dt} \int_0^L u(x, t) dx = f|_{x=0,t=t} - f|_{x=L,t=t}. \tag{8}$$

Therefore, a conservative approximation to Eq. (7) is one that satisfies the discrete equivalent of Eq. (8). This is a global definition of conservation that will be used to inform the construction of our schemes. According to the argument of Ref. [18], a globally conservative method constructed from stencils with local support must also be locally conservative for some definition of local fluxes. To derive the discrete equivalent consider an approximation to the first derivative operator given by:

$$AF' = BF, \tag{9}$$

where $A$ and $B$ are coefficient matrices, $F$ is the column vector of discrete $f$ given by $[f_0, f_1, \ldots, f_N]^T$ and $F'$ is the column vector of the unknown derivative of $f$ given by $[f'_0, f'_1, \ldots, f'_N]^T$ and we have assumed a computational domain discretized with $N + 1$ points. For central (explicit) finite differences approximations, $A$ is the identity matrix. For the compact schemes considered here, $A$ is tridiagonal and must be invertible. If it is assumed that $A$ does not vary with time, the semi-discrete version of Eq. (7) becomes:

$$\frac{d}{dt} AU + BF = 0, \tag{10}$$

where $U$ is a column vector of discrete $u$ given by $[u_0, u_1, \ldots, u_N]^T$. With this, the integral in Eq. (8) can be written as the quadrature:

$$\frac{d}{dt} \sum_{i=0}^{i=N} w_i [AU]_i = - \sum_{i=0}^{i=N} w_i [BF]_i, \tag{11}$$

where the notation $[XY]_i$ indicates the $i$th element of the column vector resulting from the multiplication of the matrix $X$ with the column vector $Y$. The discrete conservation constraint can be seen more easily with a change of notation. Let $W$ be the column vector of quadrature weights, $W = [w_0, w_1, \ldots, w_N]^T$ and let a column of $B$ be denoted by $B_i$ such that $B = [B_0, B_1, \ldots, B_N]$. Using this notation, Eq. (11) can be written as:

$$\frac{d}{dt} W^T AU = -W^T BF. \tag{12}$$

It can be seen that the expression $W^T B$ is a row vector with elements $[W^T B_0, W^T B_1, \ldots, W^T B_N]$. Eq. (12) can then be written as:

$$\frac{d}{dt} W^T AU = -W^T B_0 f_0 - W^T B_N f_N - \sum_{i=1}^{i=N-1} W^T B_i f_i. \tag{13}$$

Comparing this with the continuous statement in Eq. (8) it is evident that discrete global conservation is satisfied if

$$\sum_{i=1}^{i=N-1} W^T B_i f_i = 0. \tag{14}$$

In order for this to be true for any $f_i$, each term in the sum must be zero:

$$W^T B_i = 0, \qquad \text{for all } i \in [1, N-1]. \tag{15}$$

The above condition leads to a system of $N - 1$ equations, which must be satisified for the scheme to be discretely conservative. Furthermore, any temporal discretization that can be written as:

$$AU^{n+1} = AU^n - B\Phi(F), \tag{16}$$

where $\Phi(F)$ is prescribed by the temporal discretization, will maintain the discrete conservation properties of the spatial discretization since

$$W^T A(U^{n+1} - U^n) = -W^T B\Phi(F) \tag{17}$$

$$= -W^T B_0 \Phi_0 - W^T B_N \Phi_N. \tag{18}$$

As an example, consider integrating $U$ from time level $n$ to level $n + 1$ in Eq. (10) using the classic RK4 scheme with $k = t^{n+1} - t^n$:

$$U^{1*} = U^n \tag{19}$$

$$U^{2*} = U^n - \frac{k}{2} DF^{1*} \tag{20}$$

$$U^{3*} = U^n - \frac{k}{2} DF^{2*} \tag{21}$$

$$U^{4*} = U^n - kDF^{3*} \tag{22}$$

$$U^{n+1} = U^n - D\frac{k}{6}\left(F^{1*} + 2F^{2*} + 2F^{3*} + F^{4*}\right). \tag{23}$$

where $D = A^{-1}B$ and $F^{i*} = F(U^{i*})$. It can be seen that Eq. (23) reduces to Eq. (16) with $\Phi = \frac{k}{6}\left(F^{1*} + 2F^{2*} + 2F^{3*} + F^{4*}\right)$ and thus maintains discrete conservation of $U$ in time.

While the discrete conservation constraints given by Eq. (15) give considerable flexibility in determining quadrature weights and stencil coefficients, it is a non-trivial exercise to design schemes which satisfy these constraints. Indeed, none of the existent methods against which we compare our results in Section 4 satisfy these constraints.

### 2.3. Construction of conservative schemes

In the interior of the domain, where the centered finite difference approximations given in Tables 1 and 2 are applied using a discretization with $N + 1$ points, the entries of $B_i$ are

$$B_i = [Z^{i-p}, \gamma_p, \ldots, \gamma_1, 0, -\gamma_1, \ldots, -\gamma_p, Z^{N-i-p}]^T, \tag{24}$$

where $Z^j$ is a row vector of zeros of length $j$. From this, it is evident that weights of unity are sufficient to enforce conservation on the interior scheme.

However, the interior schemes cannot be used at the first (or last) $p$ points since they would extend beyond the boundaries of the computational domain. Instead, a set of $r$ modified boundary stencils (where $r \geq p$) of order $q$ are used to close the discrete system. In general, the accuracy of the full discrete system with interior and boundary schemes will be $\min(2(p+s), q+1)$ [9]. As such, only boundary stencils which do not diminish the interior accuracy (i.e. with $q = 2(p+s) - 1$) are considered in this paper.

A stencil of order $q$ and width $t$ approximating the first derivative operator at point $i$, near the left boundary (i.e. $i < r$), can be written as:

$$\sum_{k=-s_1}^{k=s} \beta_{ik} f'_{i+k} = \frac{1}{h} \sum_{j=0}^{j=t-1} \alpha_{ij} f_j + \mathcal{O}(h^q), \tag{25}$$

where $s_1 = \min(i, s)$, $\beta_{i0} = 1$ and $t > q - s_1 - s$. The same $\beta_{ik}$ and $\alpha_{ij}$ can be used to write the modified stencils on the right boundary as:

$$\sum_{k=-s}^{k=s_1} \beta_{i,-k} f'_{N-i+k} = -\frac{1}{h} \sum_{j=0}^{j=t-1} \alpha_{ij} f_{N-j} + \mathcal{O}(h^q), \tag{26}$$

where $i = 0$ corresponds to the right boundary point. Thus, the boundary stencils form $r \times t$ sub-matrices in the corners of the otherwise skew-symmetric $\boldsymbol{B}$. For schemes with $s > 0$, the structure of $\boldsymbol{A}$ is preserved while symmetry is not.

To write $B_i$ for the boundary stencils, we note that the first interior stencil will occur at point $r$ and will span the points $[r-p, r+p]$. This allows for splitting $B_i$ into 2 different cases. To simplify the description, let $\Gamma = [\gamma_p, \gamma_{p-1}, \ldots, 0, \ldots, -\gamma_{p-1}, -\gamma_p]$ and let $\Gamma^n$ denote the last $n$ elements of $\Gamma$. With this notation, $B_i$ can be written as,

$$B_i = \begin{cases} [\alpha_{0i}, \alpha_{1i}, \ldots, \alpha_{r-1,i}, Z^{N+1-r}]^T, & \text{for } i < r - p \\ [\alpha_{0i}, \alpha_{1i}, \ldots, \alpha_{r-1,i}, \Gamma^{i+1-r+p}, Z^{N-i-p}]^T, & \text{for } r - p \leq i < t \end{cases} \tag{27}$$

In writing the columns of $\boldsymbol{B}$ in this way, it is assumed that $t \leq r + p + 1$ (i.e. the extent of the boundary stencils does not go beyond that of the first interior stencil). Other systems are certainly possible but are not considered here. Enforcing the global conservation constraints on the left boundary stencils can then be written as:

$$[w_0, w_1, \ldots, w_{r-1}, 1, 1, \ldots] B_i = 0, \qquad \text{for } 0 < i < t, \tag{28}$$

The construction of the boundary stencils given by Eqs. (25) and (26) allows an identical system to be written for the right boundary.

At this point, it is worth highlighting the free and fixed parameters in Eq (28). First, an interior scheme is chosen which fixes $s$ and $p$ and consequently $q$. These choices impose lower bounds on $r$ and $t$ but no upper bounds. Instead, $r$ and $t$ must be chosen in such a way that the system described by Eq. (28) has a solution. It is rather easy to choose $r$ and $t$ such that the system is either over determined or under determined. Therefore a procedure has been developed which consistently yields well posed systems.

First, the relation between $t$ and $r$ is fixed with $t = r + p$. With this constraint, the first interior fluid column of $\boldsymbol{B}$ given by Eq. (24) is $B_t$. We note that there are $r + p - 1$ equations in Eq. (28) and the quadrature weights only supply $r$ unknowns. As the second constraint in this procedure, we require that the other $p - 1$ unknowns come from the last boundary stencil. Thus, it is required that the coefficients $\{\alpha_{r-1,r+1}, \ldots, \alpha_{r-1,r+p-1}\}$ are free parameters. An equivalent way of stating this is that the coefficients $\{\alpha_{r-1,0}, \ldots, \alpha_{r-1,r}\}$ are sufficient to satisfy the constraints imposed by the chosen order of accuracy. The third constraint (which only impacts one of the stencils presented here), is that there be at least one free parameter in the first boundary stencil for the purpose of optimization which will be discussed in Section 3.

With these constraints, it is possible to systematically construct conservative boundary schemes with different orders. The simplest case is for explicit finite differences (i.e. $s = 0$). The boundary schemes require $2p$ points to meet the order of accuracy requirements. Based on the constraints above, boundary schemes with $r = 2p - 1$ are constructed. After enforcing conservation, there are $2(p-1)^2$ free parameters in each system. These free parameters play a critical role in the optimization strategy presented in Section 3. The coefficients are given as functions of the free parameters in easily parsed ascii text files in the accompanying Data in Brief paper, for $p = 2, 3, 4$.

For tridiagonal compact schemes, the diagonal elements $\alpha_{1,1}, \ldots, \alpha_{r-1,r-1}$ are set to zero. The diagonal elements were set to zero because the optimization procedure failed to find stable 8th order schemes when this constraint was not enforced. It is not clear if this failure is a result of the optimization strategy employed or a more fundamental limitation. The boundary schemes require $2(s+p)$ points to meet the accuracy requirements. Including the constraint of the zero diagonal elements, and taking into account the $s + s_1$ coefficients each stencil has on the left hand side of Eq. (6), each stencil requires $2p + 1$ coefficients on the right hand side of Eq. (6). The minimum $r$ which will yield the appropriate number of free parameters in the last row is $r = 2p$. The minimum $r$ required to have at least one free parameter in the first stencil is $r = p + 2$. The largest of these is chosen for the 3rd, 5th and 7th order conservative compact boundary schemes whose coefficients are given as functions of the free parameters in easily parsed ascii text files in the accompanying Data in Brief paper.

### 2.4. Stability of the non-optimized base high order conservative schemes

The simplest choice for the free parameters in the conservative schemes discussed in the previous section, and given in the accompanying Data in Brief paper, is zero. The purpose of examining this problem here is to note that all non-optimized base schemes of order greater than 4 are unstable, highlighting the need for some kind of optimization strategy that yields suitably stable schemes. To assess the stability of the schemes with all the free parameters set to zero, the Euler equations are integrated in time using the RK4 method, starting with an initially quiescent fluid with a Gaussian density distribution:

$$\rho(x, 0) = 1 + \frac{\exp(-\frac{(x-\mu)^2}{2\sigma})}{\sqrt{2\pi\sigma}}, \tag{29}$$

$$E(x, 0) = \frac{\rho^{\gamma-1}}{\gamma - 1}, \tag{30}$$

where the energy has been initialized using isentropic relations. The only physical boundary condition for this inviscid flow is that the normal component of the velocity be zero at the walls [19]. In the one-dimensional case this becomes:

$$u(0, t) = u(L, t) = 0, \tag{31}$$

where the domain is given by $x \in [0, L]$. A uniform mesh with constant spacing $h$, is used to discretize the domain with $N + 1$ points. The left and right computational boundaries are located at points 0 and $N$, respectively. The boundary conditions for this problem lead to the conservation of the total mass and energy within the domain:

$$\frac{d}{dt} \int \rho \, dx = 0, \qquad \frac{d}{dt} \int \rho E \, dx = 0. \tag{32}$$
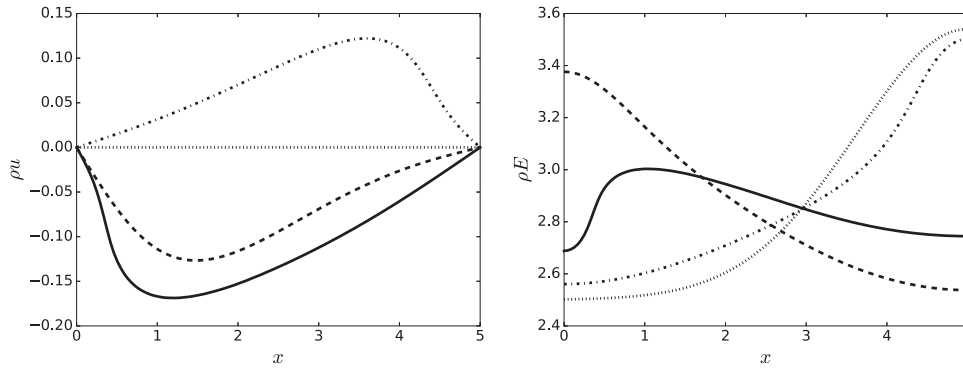
**Fig. 1.** Momentum (left) and Energy (right) at times 0, 3.2, 7.3, and 10.5 corresponding to the dotted, dashed, dash-dot and solid lines respectively. Simulation parameters are $N = 120$ and $C = 0.1$.

The use of conservative schemes ensures that these relations are satisfied discretely (to within machine precision) at finite resolutions. This is verified using the quadrature weights, $w_i$, presented with each scheme. Conversely, a non-conservative scheme is one which does not discretely satisfy these relations at finite resolutions. The timestep restriction is given by the well-known CFL constraint,

$$\Delta t = \frac{C\Delta x}{\max(|u| + a)}, \tag{33}$$

where typically $C \leq 1$. Since the equations are non-linear and there is no dissipation, infinitely thin shocks will develop. The simulations are stopped before this happens when there are still about 15 points resolving the wavefront on the coarsest grid. Simulations are performed at three different resolutions, $N = 120, 150,$ and $200$, each at different time steps with two choices for CFL constraint, $C = 0.8, 0.1$. The two choices for $C$ are considered to ensure that there are no fast or slow spurious waves contaminating the solution, which could be damped by the dissipation associated with the time integration scheme. The simulations are run with the parameters $L = 5$, $\mu = 5$, and $\sigma = 2$ until a final time of $t_f = 10.5$. The only schemes which run to completion are the 4th order explicit and compact schemes given in the accompanying Data in Brief. Snapshots of the solution at times of interest are shown in Fig. 1 for $N = 120$ and $C = 0.1$.

This particular test case was chosen due to the development of strong gradients at the boundary as the density waves are reflected. This particular test case is discussed in more detail in the next section. Again, since all non-optimized base schemes of order greater than 4 are unstable, this highlights the need for some kind of optimization strategy that yields suitably stable schemes.

### 3. Optimization for numerical stability

The idea of designing schemes with free paramters that can be chosen to enhance stability is not new. In Ref. [1], the stable 6th order scheme (the highest order devised) was found by leaving 4 free parameters in the non-conservative boundary stencils which were chosen by an eigenvalue search code. To achieve stable, high-order schemes, Ref. [11] decreased the grid spacing near the boundaries to minimize the spectral radius. The schemes developed were not conservative.

Here, a different optimization strategy is employed. Rather than attempting to optimize the schemes based on criteria which represent sufficient conditions for stability only for the linear case, the optimization is performed directly on a non-linear system of interest, the compressible Euler equations given in Eqs (1)–(3). Specifically, the one-dimensional version of these equations will be used for determining the free parameters.

The optimization procedure requires an objective function, $\theta$, to maximize. For this procedure to be successful, the value of $\theta$ must be a reasonable quantification of numerical stability. For this procedure to be efficient, $\theta$ must be relatively inexpensive to compute.

Before formally defining $\theta$, we offer a few observations on what stability means for a given non-linear system. Perhaps the most obvious observation is that a stable numerical scheme will run to some completion time, $t_c$, while an unstable numerical solution procedure will terminate before $t_c$ (assuming both meet sufficient resolution requirements). The second observation is that the stable solution procedure will yield smooth solutions while an unstable method will generate numerical oscillations.

With these observations in mind, the objective function is split into two helper functions. The first of these, $\mathcal{T}(\boldsymbol{S}, \boldsymbol{\alpha}, \boldsymbol{N}, \boldsymbol{C}, I, t_c) \to t_r$, quantifies the run time, $t_r$, of a set of simulations of the Euler equations with a particular boundary and interior scheme described by $\boldsymbol{S} = (s, p, r, t)$ and a particular set of free parameters $\boldsymbol{\alpha}$ for a set of grid resolutions, CFL numbers, and initial conditions given by $\boldsymbol{N}$, $\boldsymbol{C}$ and $I$, respectively. The computation of $t_r$ is described in Algorithm 1. Using this algorithm, it is clear that $t_r \in (0, t_c]$.

---

**Algorithm 1:** $\mathcal{T}(\boldsymbol{S}, \boldsymbol{\alpha}, \boldsymbol{N}, \boldsymbol{C}, I, t_c) \to t_r$.

---

**input** : Boundary and interior scheme parameters, $\boldsymbol{S}$
**input** : Set of free parameters, $\boldsymbol{\alpha}$
**input** : Set of grid resolutions for spatial discretization, $\boldsymbol{N}$
**input** : Set of CFL constraints for temporal discretization, $\boldsymbol{C}$
**input** : Initial conditions, $I$
**input** : Completion time, $t_c$
**output**: Average run time: $t_r$

Set coefficients for derivative operator using $\boldsymbol{S}$ and $\boldsymbol{\alpha}$;
$t_r \leftarrow 0$;
**foreach** *grid resolution N of* $\boldsymbol{N}$ **do**
  Initialize simulation with $N$ grid points and initial conditions $I$;
  **foreach** *CFL number C of* $\boldsymbol{C}$ **do**
    Integrate Euler equations in time using time constraint, $C$, until a time of $t_d$ where $t_d = t_c$ if the simulation completed successfully or $t_d < t_c$ if the simulation diverged at $t_d$;
    $t_r \leftarrow t_r + t_d$;
  **end**
**end**
$t_r \leftarrow t_r/(|\boldsymbol{N}||\boldsymbol{C}|)$;

---

The second helper function, $\mathcal{E}(\boldsymbol{S}, \boldsymbol{\alpha}, \boldsymbol{N}, \boldsymbol{C}, I, t_c, \boldsymbol{R}) \to \epsilon$, quantifies the solution smoothness for the time and space interval specified by $\boldsymbol{R}$. To be able to identify numerical oscillations in the solution,

we make use of the monotonic nature of the energy per unit volume, $\rho E$, near the walls at a late time ($t \in [9.5, 10.5]$) when the initial density, $\rho_I$ and energy, $E_I$, are given by Eqs. (29) and (30), respectively, with $\sigma = 2$ and $\mu = L = 5$. The monoticity of the energy at the final time of $t = 10.5$ can be seen in Fig 1. Thus, for a grid with $N + 1$ points, the monotonicity error on the left and right boundaries is defined as:

$$\mathcal{M}_L^m(f) = |TV_0^m(f) - (f_{m+1} - f_0)| \tag{34}$$

$$\mathcal{M}_R^m(f) = \left|TV_{N-m}^N(f) - (f_{N-m} - f_{N+1})\right|. \tag{35}$$

where total variation is given by:

$$TV_j^k(f) = \sum_{i=j}^{i=k} |f_{i+1} - f_i|, \tag{36}$$

and $f_i$ is the computed solution at point $i$. Note that $\mathcal{M}_L^m$ has been defined for a monotonically increasing function and $\mathcal{M}_R^m$ has been defined for a monotonically decreasing function to reflect the different behavior of $\rho E$ near the left and right boundaries, respectively. With these definitions, the procedure for computing $\epsilon$ is given in Algorithm 2. Typically, $\epsilon \in [10^{-7}, 10^{-5}]$ for successfully

---

**Algorithm 2:** $\mathcal{E}(\boldsymbol{S}, \boldsymbol{\alpha}, \boldsymbol{N}, \boldsymbol{C}, I, t_c, \boldsymbol{R}) \to \epsilon$.

**input** : Boundary and interior scheme parameters, $\boldsymbol{S}$
**input** : Set of free parameters, $\boldsymbol{\alpha}$
**input** : Set of grid resolutions for spatial discretization, $\boldsymbol{N}$
**input** : Set of CFL constraints for temporal discretization, $\boldsymbol{C}$
**input** : Initial conditions, $I$
**input** : Completion time, $t_c$
**input** : Space-time interval for smoothness calculations, $\boldsymbol{R} = (t_s, t_e, m)$
**output**: Maximum monotonicity error: $\epsilon$

Set coefficients for derivative operator using $\boldsymbol{S}$ and $\boldsymbol{\alpha}$;
$\epsilon \leftarrow 0$;
**foreach** *grid resolution N of $\boldsymbol{N}$* **do**
   Initialize simulation with $N$ grid points and initial conditions $I$;
   **foreach** *CFL number C of $\boldsymbol{C}$* **do**
      Integrate Euler equations in time using time constraint, $C$, until a time of $t_d$ where $t_d = t_c$ if the simulation completed successfully or $t_d < t_c$ if the simulation diverged at $t_d$;
      **if** $t_d < t_c$ **then**
         $\epsilon \leftarrow$ SENTINEL;
         **return**;
      **end**
      $\epsilon_L \leftarrow$ temporal average of $\mathcal{M}_L^m(\rho E)$ over time interval $t \in [t_s, t_e]$;
      $\epsilon_R \leftarrow$ temporal average of $\mathcal{M}_R^m(\rho E)$ over time interval $t \in [t_s, t_e]$;
      $\epsilon \leftarrow \max(\epsilon, \epsilon_L + \epsilon_R)$;
   **end**
**end**

---

optimized stencils.

The objective function $\theta(\boldsymbol{S}, \boldsymbol{\alpha}, \boldsymbol{N}, \boldsymbol{C}, I, t_c, \boldsymbol{R}) \to \nu$ (where $\nu$ is a measure of the error $\epsilon$) can then be defined in terms of $\mathcal{T}$ and $\mathcal{E}$ and is given in Algorithm 3. With this, the optimization problem is stated as: For a given stencil, $\boldsymbol{S}$, set of grid resolutions, $\boldsymbol{N}$, set of temporal resolutions $\boldsymbol{C}$, initial conditions, $I$, completion time, $t_c$ and interval for smoothness calculations, $\boldsymbol{R}$, choose $\boldsymbol{\alpha}$ such that $\theta$ is maximized. The parameters used for optimization in the present

---

**Algorithm 3:** $\theta(\boldsymbol{S}, \boldsymbol{\alpha}, \boldsymbol{N}, \boldsymbol{C}, I, t_c, \boldsymbol{R}) \to \nu$.

**input** : Boundary and interior scheme parameters, $\boldsymbol{S}$
**input** : Set of free parameters, $\boldsymbol{\alpha}$
**input** : Set of grid resolutions for spatial discretization, $\boldsymbol{N}$
**input** : Set of CFL constraints for temporal discretization, $\boldsymbol{C}$
**input** : Initial conditions, $I$
**input** : Completion time, $t_c$
**input** : Space-time interval for smoothness calculations, $\boldsymbol{R} = (t_s, t_e, m)$
**output**: Quantification of stability: $\nu$

$\nu \leftarrow \mathcal{T}(\boldsymbol{S}, \boldsymbol{\alpha}, \boldsymbol{N}, \boldsymbol{C}, I, t_c)$;
$\epsilon \leftarrow \mathcal{E}(\boldsymbol{S}, \boldsymbol{\alpha}, \boldsymbol{N}, \boldsymbol{C}, I, t_c, \boldsymbol{R})$;
**if** $\epsilon \neq$ *SENTINEL* **then** $\nu \leftarrow \nu + \log(1/\epsilon)$;

---

**Table 3**
Enumeration of search space for a given stencil defined by $\boldsymbol{S}$.

| $\boldsymbol{S} = (s, p, r, t)$ | $\boldsymbol{\alpha}$ |
|---|---|
| (0, 2, 3, 5) | $\alpha_{04}, \alpha_{14}$ |
| (0, 3, 5, 8) | $\alpha_{06}, \alpha_{16}, \alpha_{26}, \alpha_{36}, \alpha_{37}$ |
| (0, 4, 7, 11) | $\alpha_{08}, \alpha_{18}, \alpha_{28}, \alpha_{38}, \alpha_{48}, \alpha_{58}, \alpha_{59}$ |
| (1, 1, 3, 4) | $\alpha_{03}, \alpha_{13}$ |
| (1, 2, 4, 6) | $\alpha_{05}, \alpha_{15}, \alpha_{25}$ |
| (1, 3, 6, 9) | $\alpha_{07}, \alpha_{17}, \alpha_{27}, \alpha_{37}, \alpha_{47}, \alpha_{48}$ |

paper are:

$$\boldsymbol{N} = \{120, 150, 200\} \tag{37}$$

$$\boldsymbol{C} = \{0.8, 0.1\} \tag{38}$$

$$I = (\rho_I, E_I, \sigma = 2, \mu = 5, L = 5) \tag{39}$$

$$t_c = 10.5 \tag{40}$$

$$\boldsymbol{R} = (t_s = 9.5, t_e = t_c, m = 10) \tag{41}$$

The equations are integrated in time using the RK4 method. The stopping time of $t_c = 10.5$ was chosen such that the solution to the Euler equations remained continuous. If one was interested in optimizing boundary schemes for shock capturing methods, the interior schemes need to be changed appropriately and the simulation could be allowed to run further to where it would naturally develop discontinuities. Thus, the optimization procedure presented here could also be applied to shock capturing schemes.

In general, the cost of the optimization procedure grows exponentially with $|\boldsymbol{\alpha}|$. Therefore, to limit the cost, only a subset of the free parameters were included in the search space while the rest were set to zero. Table 3 shows the non-zero free parameters used to define the search space $\boldsymbol{\alpha}$ for each of the schemes considered. A gradient ascent method was used with these search spaces to find optimized schemes. To start the searches, $\boldsymbol{\alpha}$ was initialized with random numbers in the range $[-1, 1]$.

The outcome of this process is a set of stencils which perform well on the 1D Euler test. This set is then subjected to the linear and non-linear tests presented in the next section. Schemes which perform well on all tests are collected into the databases in the accompanying Data in Brief paper. The number of boundary schemes of each type are given in Table 4. The schemes analyzed in the next section are simply the first entries in the databases. The coefficients for the schemes examined in the next section are shown

**Table 4**

Number of optimized sets of boundary coefficients found for each scheme.

| Scheme family | E4 | E6 | E8 | T4 | T6 | T8 |
|---|---|---|---|---|---|---|
| Number found | 101 | 16 | 3 | 1079 | 16 | 25 |

in Tables 5 and A.6–A.10. The schemes *E*4, *E*6 and *E*8 are explicit schemes with boundary/interior orders of 3/4, 5/6, and 7/8, respectively. The expected order of accuracy for these stencils is 4, 6, and 8, respectively. The schemes *T*4, *T*6, and *T*8 are compact schemes with a tridiagonal structure with boundary/interior orders of 3/4, 5/6, and 7/8, respectively. The expected order of accuracy for these stencils is 4, 6, and 8 respectively. As an example, *T*8 is given in Table 5 rather than the Appendix.

We do not claim that the objective function described above or the particular choice of parameters for the simulation of the Euler equations is optimal. Indeed, it is difficult even to define what optimal means since the procedure yields a variety of stable schemes which behave differently for different tests. The question of how best to search for a stable scheme with a particular set of properties is very interesting but is beyond the scope of the present work. Nevertheless, the schemes presented here pass the numerical tests usually considered in the literature, including more stringent versions of these tests, which, as far as we know, no existent high order, conservative boundary schemes pass without requiring artificial dissipation, filtering, weak boundary condition enforcement or a significant reduction of the order at the boundaries.

## 4. Results

In this section, the optimized conservative schemes are subjected to a variety of tests to demonstrate stability (both Lax and asymptotic) for a variety of cases which are representative of the challenges encountered by high fidelity, DNS-like simulations. It was found that the optimized schemes perform well for the full Navier-Stokes equations. Due to the stabilizing impact of viscosity, these tests were left out in favor of purely hyperbolic problems to highlight the robustness of the optimized conservative schemes. It should also be noted that only problems with impenetrable walls, or supersonic inflow/outflow are simulated. We have not addressed the issues encountered with subsonic inflow/outflow which necessitate the use of artificial boundary conditions [2]. This was done to focus on the stability of the numerical scheme rather than the efficacy of a particular boundary treatment. The optimized schemes can certainly be applied to subsonic inflow/outflow problems but that is beyond the scope of the present work.

The first test is presented in Section 4.1 where the eigenvalues of the discretization matrices constructed from the optimized schemes are analyzed for asymptotic stability. In Section 4.2, the time stability of the schemes is demonstrated by solving a neutrally stable hyperbolic system for long times. In Section 4.3, the time stability of the schemes is demonstrated by solving the two-dimensional scalar wave equation with varying coefficients for long times. The long-time behavior of the schemes in the presence of significant point-to-point variations in error is assessed with an inviscid vortex problem in Section 4.4. The final test in Section 4.5 is a two-dimensional extension of the test used for optimization and demonstrates the smoothness of the solution even as the scales of the solution change drastically with time.

In addition to testing each the optimized conservative schemes developed in the previous section, three other existing schemes are tested for comparison. The first scheme is an explicit 5th order boundary scheme developed by Carpenter et al. [1], which was found via an eigenvalue search process. This scheme will be referred to as *S*1 and the coefficients are given in Table B.11. The interior uses the 6th order compact scheme in Table 2 with $(s, p) = (1, 2)$

The second scheme, *S*2, is a 5th order compact scheme due to Cook and Riley [12] and given in Table B.12. This scheme is coupled with the 6th order compact scheme in Table 2 with $(s, p) = (1, 2)$.

The third scheme, *S*3, given in Table B.13 was developed by Turner et al. [14] and has been optimized in Fourier space for spectral accuracy. The boundary scheme is coupled with the optimized 4th order interior scheme of Kim [20] which is given Table B.14.

The schemes *S*2 and *S*3 are used with a high order filter for stability purposes by their respective authors. No filtering is used in the present work, in order to make a fair comparison between the schemes and test their properties without stabilizing source terms.

For schemes, *S*1–*S*3, the discrete conservation constraints given by Eq. (12) cannot be discretely satisfied for the given coefficients for any set of quadrature weights, $w_i$. For example, applying the conservation constraints to scheme *S*2 results in the following overdetermined system for the left boundary quadrature weights:

$$7w_2 + 3w_1 + 21w_0 - 7 = 0,$$
$$196w_2 - 18w_1 - 168w_0 - 203 = 0,$$

**Table 5**

Scheme *T*8: optimized boundary coefficients for conservative 7th order compact first derivative approximation with 8th order tridiagonal interior scheme.

| | | |
|---|---|---|
| $w_0 = 0.5623384360774939$ | $w_1 = -0.01354322834668401$ | $w_2 = 0.4905160476934302$ |
| $\beta_{0,1} = 3.210113927329531$ | $\beta_{1,-1} = 2.21110473043239$ | $\beta_{2,-1} = 1.557633196122124$ |
| $\alpha_{00} = -3.051444846761362$ | $\beta_{1,1} = 42.08319933908019$ | $\beta_{2,1} = 6.482610425055064$ |
| $\alpha_{01} = 2.345334805372179$ | $\alpha_{10} = -4.873954900119216$ | $\alpha_{20} = -0.2604486511132088$ |
| $\alpha_{02} = -0.8696582180114061$ | $\alpha_{12} = -53.18177248515291$ | $\alpha_{21} = -1.943640425204907$ |
| $\alpha_{03} = 3.641381848342838$ | $\alpha_{13} = 93.4348874201782$ | $\alpha_{23} = -3.84806892990241$ |
| $\alpha_{04} = -3.399810121117448$ | $\alpha_{14} = -52.74983250718357$ | $\alpha_{24} = 8.245332418591937$ |
| $\alpha_{05} = 1.792414554502852$ | $\alpha_{15} = 22.56437298084277$ | $\alpha_{25} = -2.779674691274779$ |
| $\alpha_{06} = -0.5246438812007604$ | $\alpha_{16} = -5.886555463761137$ | $\alpha_{26} = 0.6603673342280958$ |
| $\alpha_{07} = 0.0664258588731064$ | $\alpha_{17} = 0.692854955195867$ | $\alpha_{27} = -0.0738670553247296$ |
| $w_3 = -0.6567072566895262$ | $w_4 = -0.04274750710778264$ | $w_5 = 1.590322461525674$ |
| $\beta_{3,-1} = -1.329341564172446$ | $\beta_{4,-1} = -1.213703810247279$ | $\beta_{5,-1} = -0.1776191023391513$ |
| $\beta_{3,1} = -2.465569273620743$ | $\beta_{4,1} = 1.660769542489766$ | $\beta_{5,1} = 0.2232924886469337$ |
| $\alpha_{30} = -0.05878600824425402$ | $\alpha_{40} = 0.05619441751764617$ | $\alpha_{50} = -0.005353093751500729$ |
| $\alpha_{31} = 0.7074851396321982$ | $\alpha_{41} = -0.4761142198435586$ | $\alpha_{51} = 0.04953262252336028$ |
| $\alpha_{32} = -0.2983532234844736$ | $\alpha_{42} = 1.967293657743868$ | $\alpha_{52} = -0.2157074945553577$ |
| $\alpha_{34} = 1.491392318405186$ | $\alpha_{43} = -2.297921866880887$ | $\alpha_{53} = 0.6319138819385537$ |
| $\alpha_{35} = -2.222455418896595$ | $\alpha_{45} = -0.7202751534930111$ | $\alpha_{54} = -1.144234713147819$ |
| $\alpha_{36} = 0.4240020577097782$ | $\alpha_{46} = 1.865337479238859$ | $\alpha_{56} = 0.6783115550998231$ |
| $\alpha_{37} = -0.0432848651218399$ | $\alpha_{47} = -0.447823643536206$ | $\alpha_{57} = 0.00541430607170 6973$ |
| | $\alpha_{48} = 0.0533093292532889$ | $\alpha_{58} = 1.229358212328832e - 4$ |
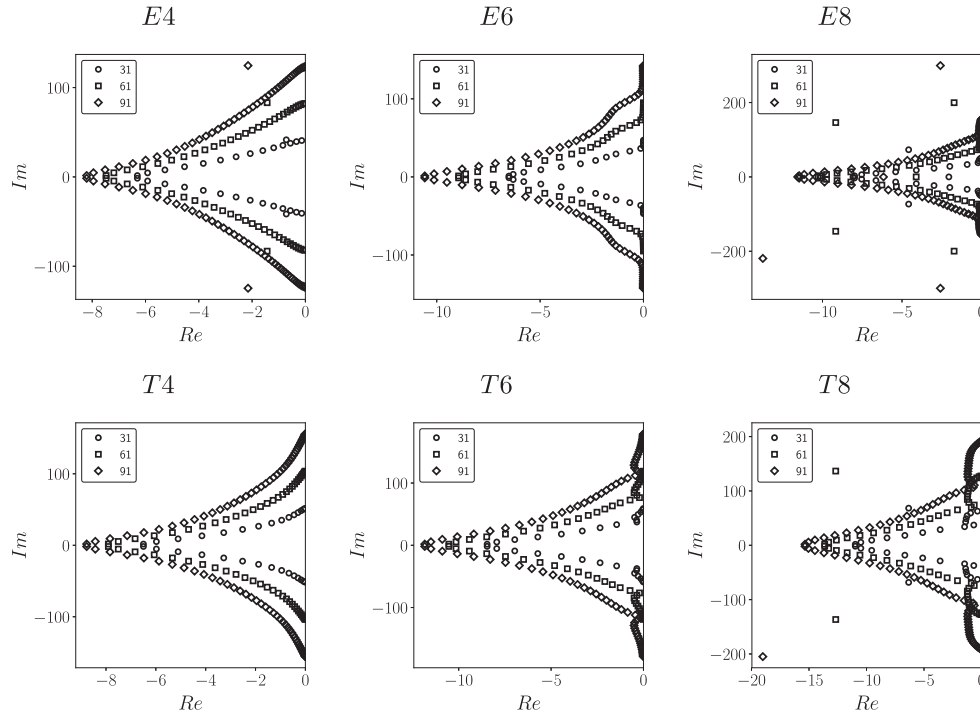
**Fig. 2.** Real and Imaginary parts of eigenvalues of discretization matrix for all optimized conservative schemes as indicated. The results of several different grid resolutions are shown. The real parts of all eigenvalues are negative.

$$216w_1 + 756w_0 - 203 = 0,$$
$$196w_2 + 30w_1 - 168w_0 + 7 = 0,$$

which does not admit solutions. The same holds true for schemes $S1$ and $S3$.

### 4.1. Asymptotic stability: eigenvalue analysis

In ref. [1], the importance of asymptotic stability for long time simulations was noted. An asymptotically stable scheme is one for which the error does not grow unphysically with time. To illustrate, consider the linear hyperbolic equation:

$$\frac{\partial u}{\partial t} + \frac{\partial u}{\partial x} = 0, \qquad \text{for } 0 \leq x \leq 1, \text{and } t \geq 0, \tag{42}$$

with consistent initial and boundary conditions for $u = u(x,t)$

$$u(x,0) = f(x) \qquad u(0,t) = g(t). \tag{43}$$

Assuming a spatial discretization of $N+1$ points, the first derivative operator can be approximated as:

$$AU' = BU, \tag{44}$$

where $A$ and $B$ are of dimension $(N+1) \times (N+1)$ and $U, U'$ are column vectors of length $N+1$. The fully discrete solution procedure involves solving Eq. (44) over the whole domain and updating $U$ accordingly, except at the boundary where $u(0,t) = g(t)$ is imposed. Let $D = -A^{-1}B$, and let the $N \times N$ submatrix of $D$ which does not include the first row or column of $D$, be denoted by $Q$. With this notation, the semi-discrete system for $\hat{U} = [u_1, u_2, \ldots, u_N]^T$ can be written as:

$$\frac{d\hat{U}}{dt} = Q\hat{U} + G, \tag{45}$$

where $G$ is a column vector of length $N$ giving the appropriate weights of the stencils on the boundary point, $u_0$. The stability of this semi-discrete system is governed by the eigenvalues, $\lambda$, of the spatial discretization matrix, $Q$. Let the real and imaginary parts of

an eigenvalue be given by $\mathrm{Re}(\lambda)$ and $\mathrm{Im}(\lambda)$, respectively. The semi-discrete system is then stable if [21]

$$\mathrm{Re}(\lambda) \leq 0 \qquad \text{for all } \lambda. \tag{46}$$

The discretization matrix $Q$ can be constructed for any scheme by consulting Tables A.6–5. Fig. 2 shows the real and imaginary parts of the eigenvalues of $Q$ for schemes $E4$, $E6$, $E8$, $T4$, $T6$, and $T8$ for $N+1 = 31, 61, 91$. The real parts of all eigenvalues are negative, satisfying the stability constraint given by Eq (46). In all schemes, no eigenvalues with positive real parts are found, indicating asymptotic stability [1]. The same holds true for every scheme in the accompanying Data in Brief paper.

### 4.2. Time stability: constant coefficient hyperbolic system

In this section, the accuracy and time stability of the schemes is demonstrated by solving the neutrally stable hyperbolic system describing a standing wave:

$$\frac{\partial u}{\partial t} = \frac{\partial v}{\partial x}, \qquad \frac{\partial v}{\partial t} = \frac{\partial u}{\partial x}, \quad x \in [0,1], \tag{47}$$

with boundary conditions:

$$u(0,t) = 0, \quad v(1,t) = 0. \tag{48}$$

The initial conditions chosen for this test case are:

$$u(x,0) = -\frac{3\pi}{2} \sin \frac{3\pi x}{2}, \quad v(x,0) = 0, \tag{49}$$

which yield the exact solution:

$$u(x,t) = -\frac{3\pi}{4} \left[ \sin \frac{3\pi(x-t)}{2} + \sin \frac{3\pi(x+t)}{2} \right], \tag{50}$$

$$v(x,t) = \frac{3\pi}{4} \left[ \sin \frac{3\pi(x-t)}{2} - \sin \frac{3\pi(x+t)}{2} \right] \tag{51}$$
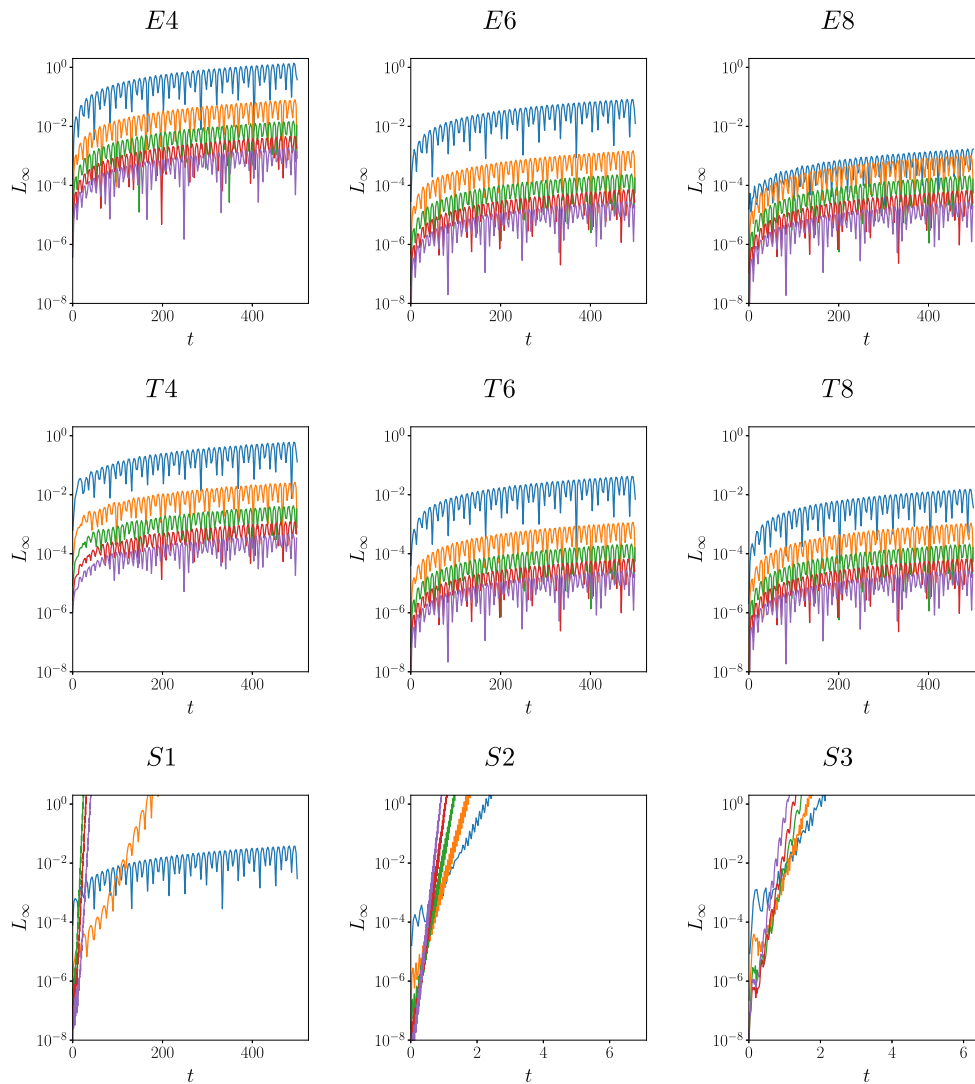
**Fig. 3.** $L_\infty$ norm of error in $u$ over $0 \le t \le 500$, for $N \in \{21, 41, 61, 81, 101\}$ corresponding to the colors blue, orange, green, red, and purple, respectively, and $CFL = 0.5$, for the hyperbolic system in Section 4.2. The optimized schemes developed in this paper behave well at all grids. The comparison schemes, $S1$, $S2$, and $S3$ are unstable on multiple grids. (For interpretation of the references to colour in this figure legend, the reader is referred to the web version of this article.)

For this test, domain sizes of $N = 21, 41, 61, 81, 101$ are used with two different time step constraints: constant CFL and constant time step, $\Delta t$. The constant CFL tests are run with CFL $= \Delta t / \Delta x = 0.5$ to demonstrate that the schemes yield appropriate results for reasonable timesteps. A timestep of $\Delta t = 0.001$ was used for the constant timestep case corresponding to a CFL $= 0.1$ on the finest grid. The tests are run until $t = 500$. This run-time is comparable to others reported in the literature [22]. Note that in these previous works, no schemes with direct boundary condition enforcement were able to pass this stringent numerical test. Rather, for small CFLs, the solutions would diverge very quickly (i.e $t < 5$). Integration in time is done using the standard RK4 method.

Fig. 3 shows the $L_\infty$ norm of the error in $u$ as a function of time for the constant CFL case for the indicated scheme. The optimized schemes, $E4$, $E6$, $E8$, $T4$, $T6$, and $T8$ all behave in a stable manner on all grid resolutions indicating time stability for this stringent numerical test. The comparison schemes $S1$, $S2$, and $S3$ all diverge from the true solution very rapidly on multiple grids. It is interesting to note that $S1$ does exhibit stable behavior on one grid and a particular choice of CFL. This highlights the need to perform such numerical tests on a broad spectrum of temporal and spatial resolutions.

Holding the timestep constant at a small value allows for determining the order of accuracy of the spatial schemes. To this end, the maximum error in $u$ recorded over the course of the simulation is reported as $L_\infty(u)$ in Fig. 4 for the different schemes as a function of $N$. Lines indicating the expected order of the schemes are drawn on each plot. The optimized schemes all behave in a stable manner and yield the expected order of convergence. Due to the long time integration, the error bottoms out around $10^{-8}$. This behavior is only visible for the $T6$ and $T8$ schemes due to their very low discretization errors. Error norms for all schemes at different CFLs and constant $\Delta t$ are recorded in the accompanying database.

## 4.3. Time stability: two-dimensional varying coefficient scalar wave equation

In this section, the accuracy and long-time stability of the schemes is demonstrated by solving the two-dimensional, varying coefficient, scalar wave equation:

$$\frac{\partial u}{\partial t} + c_x \frac{\partial u}{\partial x} + c_y \frac{\partial u}{\partial y} = 0, \qquad 0 \le (x, y) \le L, \quad t \ge 0, \qquad (52)$$
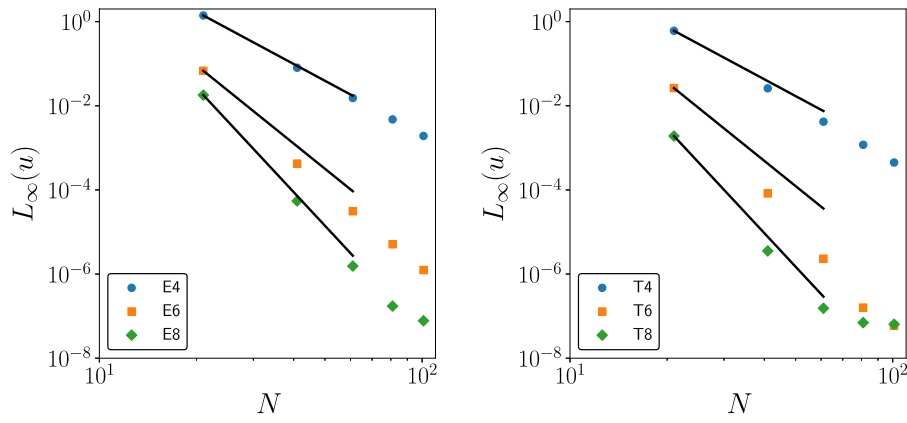
**Fig. 4.** Maximum error in $u$ over $0 \leq t \leq 500$, $L_\infty(u)$, plotted against grid size, $N$, for $\Delta t = 0.001$ and indicated schemes. The expected order of each scheme is drawn as a solid black line. The error bottoms out around $10^{-8}$.
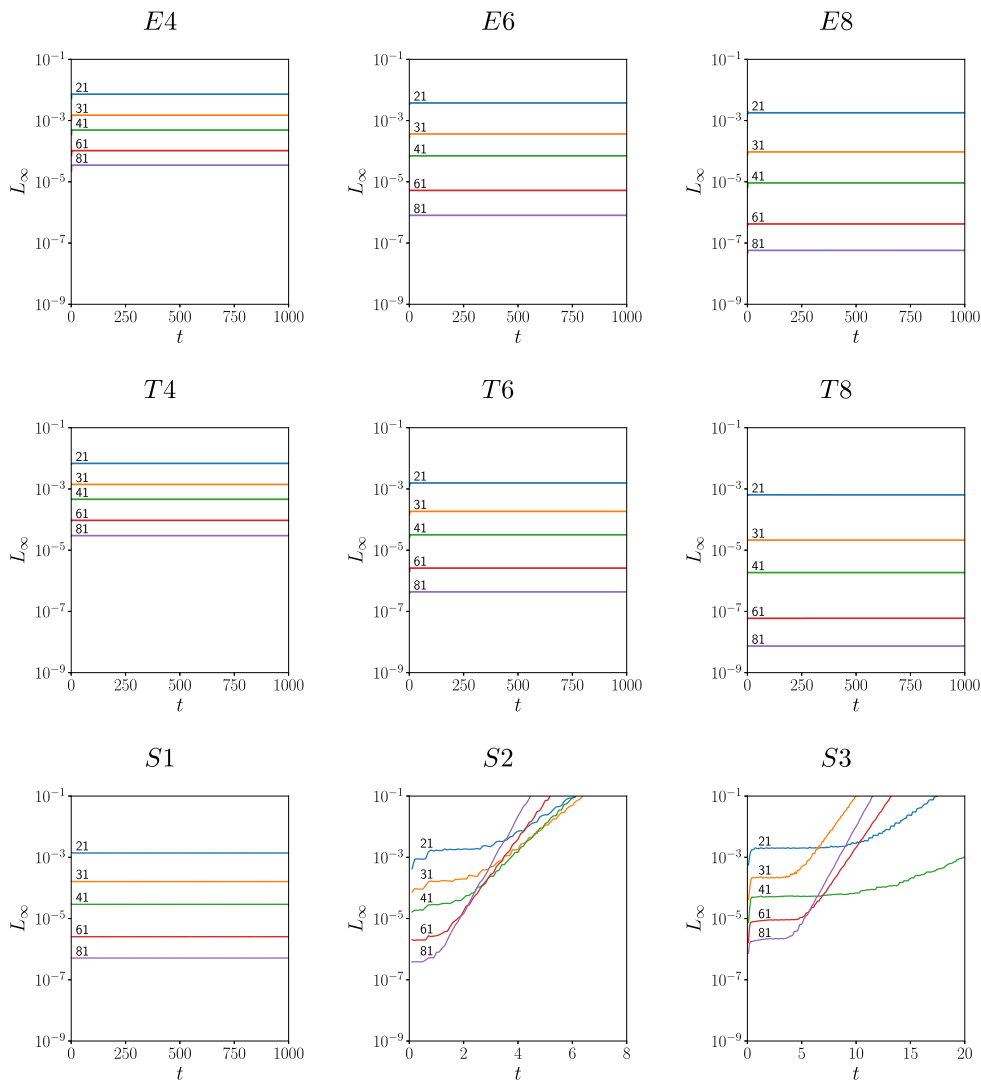


**Fig. 5.** $L_\infty$ norm of error over $0 \leq t \leq 1000$, for indicated $N$ and constant timestep of $\Delta t = 0.001$ for the varying coefficient scalar wave equation test in Section 4.3. The optimized schemes developed in this paper as well as $S1$ exhibit time stability.

where,

and initial and boundary conditions for $u = u(x, y, t)$,

$$u(x, y, 0) = \sin 2\pi \psi, \tag{54}$$

$$c_x = \frac{\partial \psi}{\partial x}, \quad c_y = \frac{\partial \psi}{\partial y}, \quad \psi(x, y) = \sqrt{(x + 0.25)^2 + (y + 0.25)^2},$$

$$\tag{53}$$

$$u(0, y, t) = \sin 2\pi (\psi(0, y) - t) \tag{55}$$
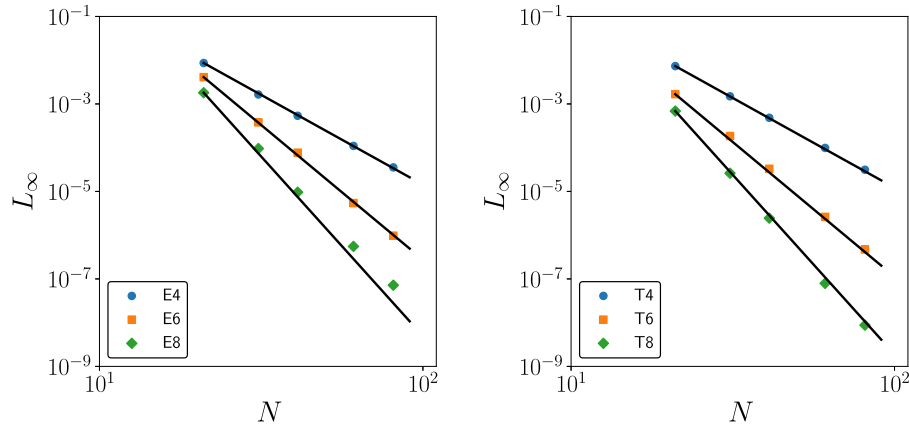
**Fig. 6.** Maximum error over $980 \leq t \leq 1000$, $L_\infty$, plotted against grid size, $N$, for $\Delta t = 0.001$ and indicated schemes. The expected order of each scheme is drawn as a solid black line.

$$u(x, 0, t) = \sin 2\pi (\psi(x, 0) - t). \tag{56}$$

The exact solution is a circular wave radiating outward from $(-0.25, -0.25)$, given by

$$u(x, y, t) = \sin 2\pi (\psi - t). \tag{57}$$

We define the period, $T$, of the solution as the time it takes for the wave to travel from the origin to $(L, L)$. The domain length $L$ is chosen to be $L = \sqrt{2}$ such that $T = 2$.

For this test, grid sizes of $N = 21, 31, 41, 61, 81$ in each direction are again used with two different time step constraints: constant CFL and constant time step, $\Delta t$. The constant CFL tests are run with CFL $= \Delta t / \Delta x = 0.8$ to demonstrate that the schemes yield appropriate results for reasonable timesteps. A timestep of $\Delta t = 0.001$ was used for the constant timestep case corresponding to a CFL of roughly 0.06 on the finest grid. To demonstrate time stability, the tests are run for a full 500 periods (until $t = 1000$).

Fig. 5 shows the $L_\infty$ norm of the error as a function of time for the constant $\Delta t$ case for the indicated scheme. The error does not grow in time but simply oscillates about a constant mean with the same period as the exact solution after a brief transient for the optimized conservative 4th, 6th and 8th order schemes developed in Section 3. The $S1$ comparison scheme is also stable for this long running test but $S2$ and $S3$ are not. The results for the constant CFL case are qualitatively similar and are available in the accompanying Data in Brief paper.

Holding the timestep constant at a small value allows for determining the order of accuracy of the spatial schemes. To this end, the maximum error recorded over the final 10 periods is reported as $L_\infty$ in Fig. 6 for the different schemes and timestep constraints as a function of $N$. A line indicating the expected order of each scheme is drawn on the plots. The optimized 4th, 6th and 8th order schemes developed in this paper all exhibit the desired order of accuracy.

### 4.4. Nonlinear test: inviscid vortex/numerical reflection

In this section the two-dimensional Euler equations are solved in order to examine the transport of an inviscid vortex through a domain and it's numerical collision with a supersonic outflow boundary. This collision with the outflow boundary generates very high frequency errors which propagate back into the domain with the potential to destabilize the simulation over long periods of time. The transport of an inviscid vortex through a periodic domain has been studied to quantify the impact of dissipation in upwinded schemes (e.g., Ref. [23]). The supersonic inflow/outflow case has been examined in Refs. [14,20] for relatively short times

(1.5 flow through times based on the background streamwise velocity). In the present case, the simulations are run for 50 flow through times with supersonic inflow/outflow in the streamwise direction. Periodic boundary conditions are imposed in the cross-stream direction.

We adopt the notations from Ref. [14] to describe the analytic solution for a vortex of nondimensional circulation, $\epsilon$, propagating in the $x$ direction. The solutions are repeated below for convenience:

$$\frac{\rho}{\rho_\infty} = \left(1 - \frac{(\gamma - 1)}{2}\psi^2\right)^{1/(\gamma - 1)}, \tag{58}$$

$$\frac{u}{a_\infty} = M_\infty + Ky\psi, \tag{59}$$

$$\frac{v}{a_\infty} = -Kx\psi, \tag{60}$$

$$\frac{p}{p_\infty} = \left(\frac{\rho}{\rho_\infty}\right)^\gamma, \tag{61}$$

where $\psi = \frac{\epsilon}{2\pi} \exp((1 - K^2(x^2 + y^2))/2)$, $M_\infty$ is the free stream Mach number, and $\gamma = c_p/c_v = 1.4$. As with the previous tests, time integration is carried out using a standard RK4 method. The tests were run on a computational domain of $x \in [0, 20]$, $y \in [0, 10]$ with $(x_0, y_0) = (10, 5)$, $K = 1$, $\epsilon = 1.5$ and $M_\infty = 2.0$

All schemes were tested on four different grid resolutions, $N_x \times N_y = 51 \times 26$, $101 \times 51$, $201 \times 101$, and $401 \times 201$ with two different timesteps, $C = 0.8, 0.1$ until a time of $t = 1000$ (50 flow through times).

To illustrate the numerical stability issues, early time results with $T8$ are shown in Fig. 7, which depicts contours of the pressure at times $t = 0, 5$, and 10 for the different grid resolutions. Half of the vortex has propagated through the outflow boundary by a time of $t = 10$. Wireframe plots of the error in pressure, $P_\epsilon$, are shown for the coarsest mesh in Fig. 8 at two slightly later times of $t = 11$ and $t = 23$. Large high-frequency errors appear at both the inflow and outflow boundaries as the vortex exits the domain around $t = 11$. At the later time of $t = 23$, the point-to-point oscillations in $P_\epsilon$ are more pronounced. However, all the optimized conservative schemes developed in Section 3 are stable to these kinds of perturbations. The evolution of the infinity norm of the pressure error, $L_\infty(P_\epsilon)$ over time using the $T8$ scheme is shown in Fig. 9. The peak of the error occurs around time $t = 10$. After this, the error exhibits complex behavior as high frequency error waves bounce back and forth between the inflow and outflow boundaries before ultimately decaying. The magnitude of the peak error does
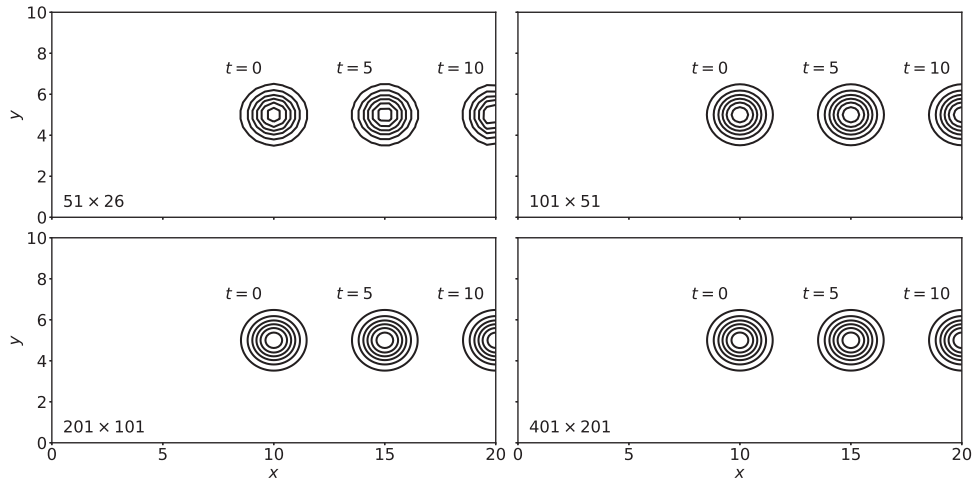
**Fig. 7.** Pressure contours of the solution computed with the 8th order *T8* scheme at times $t = 0, 5, 10$ as the vortex moves from left to right at the indicated resolutions. The pressure contours are drawn at the same values for all times and grids. The contours range from 0.12 at the outer edge of the vortex to 0.18 in the interior of the vortex.
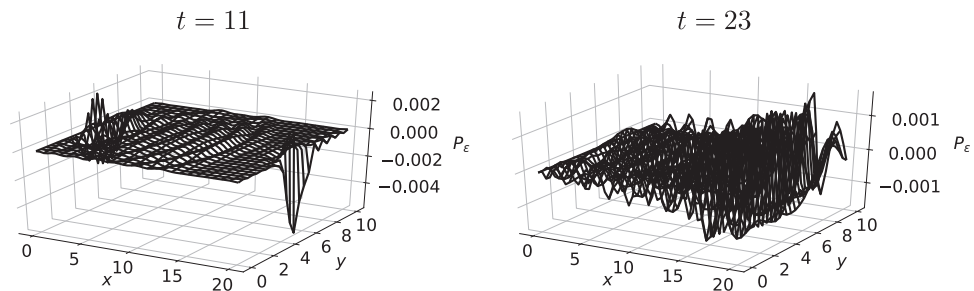


**Fig. 8.** Wireframe plot of pressure error, $P_\epsilon$, at indicated times for the solution computed with the 8th order *T8* scheme at the coarsest resolution of $51 \times 26$ points.
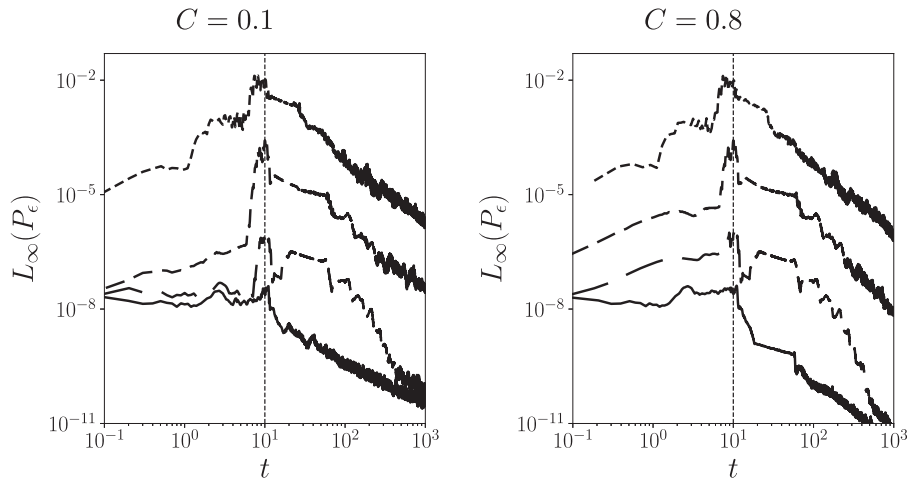


**Fig. 9.** Evolution of infinity norm of pressure error, $L_\infty(P_\epsilon)$ for the inviscid vortex simulation for the indicated time constraints with the 8th order *T8* scheme. The short, medium and long dashed lines correspond to grids with $N_x = 51, 101$, and 201, respectively. The solid lines represents the finest grid with $N_x = 401$. The vertical dashed line at $t = 10$ is when the half the vortex has left the domain through the outflow.

not appear to be affected by the size of the timestep. Due to the dissipation inherent in the RK4 with a larger timestep, the error decreases more rapidly at larger times for $C = 0.8$.

Fig. 10 shows the evolution of $L_\infty(P_\epsilon)$ for the rest of the schemes considered in the paper for $C = 0.1$. The optimized conservative schemes *E4*, *E6*, *E8*, *T4*, *T6* and *T8* all display stable, converging behavior for this challenging test problem. Note that the 8th order schemes do not offer an advantage over the 6th order schemes in this case. This may be due to the fact that higher order methods will damp fewer wave modes and therefore be more susceptible to the high frequency errors that are generated by this test. The schemes exhibit very similar behavior for the larger timestep with both the peak and final errors recorded in the ac-

companying database. *S1* also performs well on this problem while both *S2* and *S3* diverge shortly after the vortex passes through the outflow.

### 4.5. Nonlinear test: Gaussian pulse

As the final test, we solve the Euler equations for a modified version of the problem used in the optimization process. The initial conditions are given by:

$$\rho(x, y, 0) = 1 + \frac{\exp\left(-\frac{(x-L_x)^2 + (y-L_y)^2}{2\sigma}\right)}{\sqrt{2\pi\sigma}}, \tag{62}$$
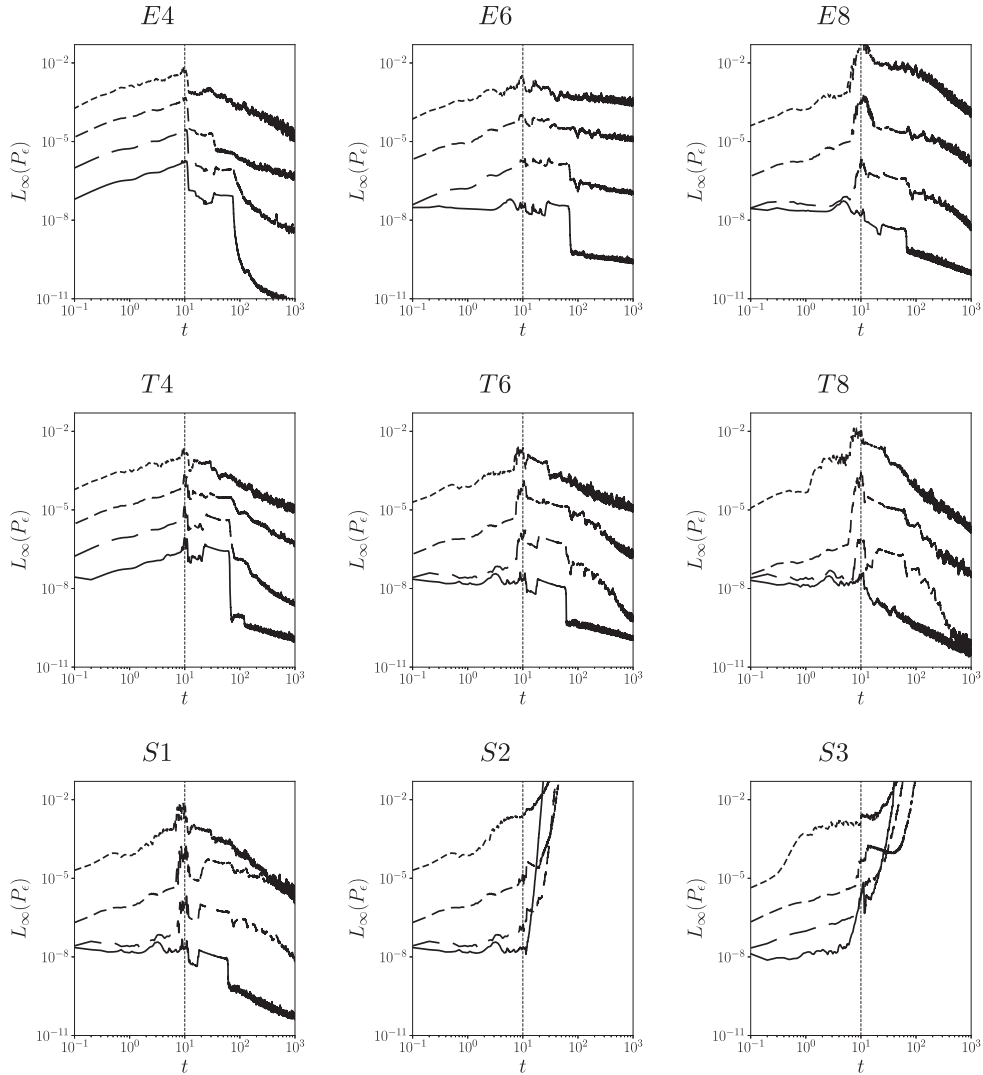
**Fig. 10.** $L_\infty$ norm of error in Pressure as a function of time, $t$. The short, medium and long dashed lines correspond to grids with $N_x = 51, 101$, and 201, respectively. The solid lines represents the finest grid with $N_x = 401$. Results are for the case with constant CFL $= 0.1$. The vertical dashed line at $t = 10$ is when the half the vortex has left the domain through the outflow.

$$u(x, y, 0) = 0 \tag{63}$$

$$v(x, y, 0) = 0 \tag{64}$$

$$E(x, y, 0) = \frac{\rho^{\gamma-1}}{\gamma - 1}, \tag{65}$$

where the energy has been initialized using isentropic relations. There are slip-walls on all 4 sides of the domain such that the boundary conditions are,

$$u(0, y, t) = u(L_x, y, t) = v(x, 0, t) = v(x, L_y, t) = 0, \tag{66}$$

where the domain is given by $x \in [0, L_x]$, $y \in [0, L_y]$. The equations are integrated in time using the RK4 method. A domain size of $L_x = L_y = 5$ is chosen with $\sigma = 2$. As in the one-dimensional case, in the absence of viscosity, the solution will develop singularities. The simulation is stopped before this occurs at a time of $t = 27$. Snapshots of the energy at $t = 0, 23$, and 27 are shown in Fig. 11 for the $T8$ scheme. The solution starts off smooth and excessively resolved but rapidly develops small scale structure that becomes

challenging to resolve as the initial pulse reflects off the walls and interacts with itself. The rapidly changing scales of the solution make it difficult to remove the time dependence and demonstrate an order of convergence consistent with the spatial scheme. Therefore, we will simply examine the smoothness of the average kinetic energy, $\langle K \rangle$, over time and demonstrate that the convergence is moving in the right direction.

The solution obtained with $T8$ on a $1441 \times 1441$ grid with a timestep of $\Delta t = 0.00015$ (corresponding to a CFL of approximately 0.05) is used as the exact solution. The average kinetic energy for this case is shown in Fig. 12. To compare with the exact solution, all schemes are run with a constant $\Delta t = 0.00015$ at grid resolutions $N_x \times N_y = 181 \times 181$, $241 \times 241$, and $361 \times 361$. The schemes yielded quantitatively similar results at a CFL of 0.5. Fig. 13 shows the error in average kinetic energy $\langle K \rangle_\epsilon$ for the 3 grid resolutions for the $T8$ scheme demonstrating stability and convergence. Virtually identical plots can be shown for $E4$, $E6$, $E8$, $T4$, $T6$, and $S1$. After short times, both $S2$ and $S3$ diverge.

At this point it is worth noting that only the optimized schemes developed in this paper pass all of the numerical stability tests. The comparison scheme, $S1$, which was designed with stability in mind, fails the test in Section 4.2. The comparison schemes, $S2$ and
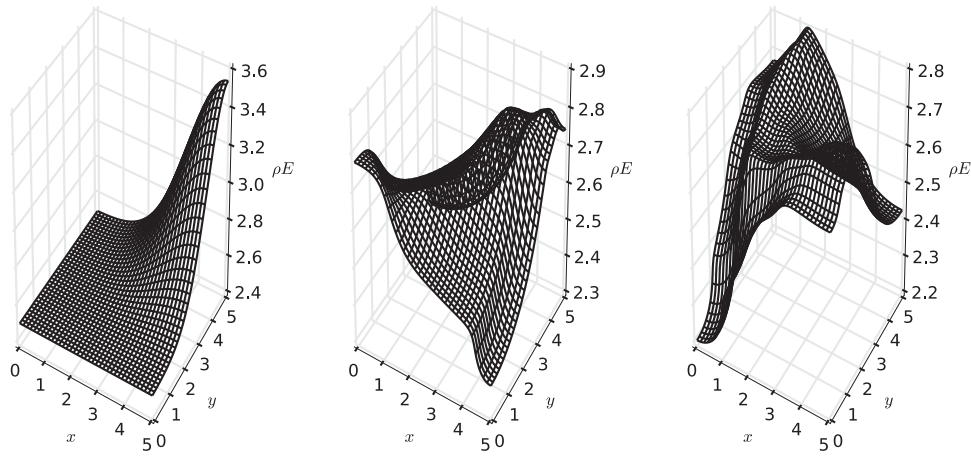
**Fig. 11.** Wireframe plot of Energy $\rho E$ computed with the 8th order $T8$ scheme at times $t = 0, 23.1, 27$ (left to right) for the initial conditions in Eq. (62).
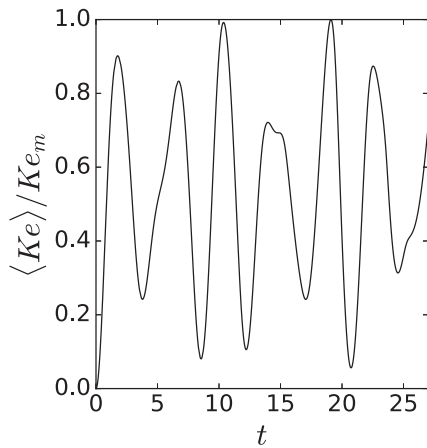


**Fig. 12.** Average kinetic energy normalize by maximum kinetic energy $Ke_m = 0.002259$ plotted against time for the 8th order $T8$ scheme on a $1441 \times 1441$ grid.
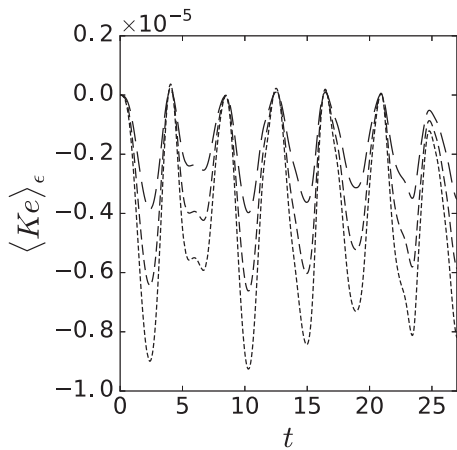


**Fig. 13.** Error in average kinetic energy for the Gaussian pulse test Section 4.5 with grids given by $Nx = 181, 241$, and $361$ corresponding to short, medium and long dashed lines, respectively. The solution is obtained using the $T8$ scheme but virtually identical plots (not shown) are obtained with $E4$, $E6$, $E8$, $T4$, $T6$, and $S1$.

$S3$, are used here without any numerical filtering and fail all of the stability tests.

It is also worth noting that these tests do not constitute a rigorous stability proof for non-linear systems of partial differential equations. The tests presented here are meant to be representative of the numerical challenges faced in performing direct numerical simulations of the Navier–Stokes equations. The optimized schemes may not be suitable for systems that exhibit very different behavior. For example, the schemes will not be stable in the presence of discontinuities.

## 5. Conclusions

The primary challenge of using high-order finite differences for high-fidelity simulations of non-linear physics in non-periodic domains lies in the construction of stable, conservative and high-order numerical boundary schemes. Existing high-order schemes, utilizing direct boundary condition enforcement, either sacrifice conservation, or require the order at the boundary to be significantly reduced, limiting their effectiveness for DNS. The schemes presented in this paper are able to achieve high-order and satisfy conservation without introducing artificial dissipation or filtering. To this end, a thorough elucidation was given of the constraints which a discretely conservative scheme must satisfy, as well as a general procedure for constructing discretizations of any order which satisfy these constraints. It was shown that this process results in numerical boundary schemes which have free coefficients that can be chosen without changing the order of accuracy of the scheme. A test of these conservative schemes with all the free parameters set to 0 was performed using the compressible Euler equations. All schemes with greater than 4th order accuracy were found to be unstable with this naive choice of free parameters. To rectify this, a novel optimization approach was developed and applied directly to the Euler equations (as opposed to a simplified linear model) to find the free parameters that would yield stable, conservative schemes of orders 4, 6, and 8. Since the focus of the present work is on continuous solutions to the governing equations, the Euler equations are only used as a stringent, zero-dissipation test case, for times small enough so that singularities do not develop during the simulation.

Parabolic terms (i.e. second order derivatives) were not investigated here because the schemes available in the literature are already stable [15] and require no optimization.

The stability and accuracy of the new conservative schemes was verified in a number of ways and compared to three popular schemes existent in the literature. None of the comparison schemes passed all of the stability tests in this work. First, an eigenvalue analysis of each scheme applied to the linear advection equation was performed which showed that all new schemes were asymptotically stable. Following this, a long-time simulation of a neutrally stable hyperbolic system was done, which demonstrated that each new scheme was stable and of the expected accuracy. Long-time simulations of the two-dimensional varying coefficient scalar wave equation demonstrated the same results. All schemes

were tested in simulating the compressible Euler equations in two different configurations. In the first configuration, a long-time simulation of an isentropic vortex passing through an outflow boundary highlighted the excellent stability and accuracy of the conservative schemes. The second configuration involved the evolution of a two dimensional Gaussian density pulse and highlighted the stability of the new schemes in problems with rapidly changing scales.

To the best of our knowledge, the 6th and 8th order schemes developed in this paper mark the first successful application of conservative finite-differences of such high order to non-linear hyperbolic initial boundary value problems without requiring artificial dissipation or filtering, while allowing for direct boundary condition enforcement.

## Acknowledgments

## Appendix A. Optimized conservative boundary schemes

The databases in the accompanying Data in Brief paper contain a number of optimized sets of boundary coefficients that can be used to simulate all the numerical tests in this paper in a stable and accurate manner. The first scheme in each database was examined in Section 4. The coefficients of each scheme used here are given in Tables 5 and A.6–A.10. The schemes $E4$, $E6$ and $E8$ are explicit schemes with boundary/interior orders of 3/4, 5/6, and 7/8, respectively. The schemes $T4$, $T6$, and $T8$ are compact schemes with a tridiagonal structure with boundary/interior orders of 3/4, 5/6, and 7/8, respectively.

**Table A.6**
Scheme $E4$: optimized boundary coefficients for conservative 3rd order first derivative approximation with 4th order interior scheme.

| | | |
|---|---|---|
| $w_0 = 0.375$ | $w_1 = 1.166666666666667$ | $w_2 = 0.9583333333333334$ |
| $\alpha_{00} = -2.606665712521815$ | $\alpha_{10} = -0.1709371632691653$ | $\alpha_{20} = 0.1846187819231725$ |
| $\alpha_{01} = 6.093329516753927$ | $\alpha_{11} = -1.149584680256672$ | $\alpha_{21} = -1.071808461026023$ |
| $\alpha_{02} = -6.139994275130892$ | $\alpha_{12} = 1.974377020385008$ | $\alpha_{22} = 0.6077126915390348$ |
| $\alpha_{03} = 3.426662850087261$ | $\alpha_{13} = -0.8162513469233387$ | $\alpha_{23} = 0.2615248723073101$ |
| $\alpha_{04} = -0.773332379188482$ | $\alpha_{14} = 0.162396170064168$ | $\alpha_{24} = 0.0179521152565058$ |

**Table A.7**
Scheme $E6$: optimized boundary coefficients for conservative 5th order first derivative approximation with 6th order interior scheme.

| | | |
|---|---|---|
| $w_0 = 0.3298611111111111$ | $w_1 = 1.320833333333333$ | $w_2 = 0.7666666666666667$ |
| $\alpha_{00} = -2.456973788821863$ | $\alpha_{10} = -0.1564337842768911$ | $\alpha_{20} = 0.14591004701167$ |
| $\alpha_{01} = 6.04184273293118$ | $\alpha_{11} = -1.344730627671987$ | $\alpha_{21} = -1.07546028207002$ |
| $\alpha_{02} = -7.604606832327949$ | $\alpha_{12} = 2.653493235846633$ | $\alpha_{22} = 1.105317371841717$ |
| $\alpha_{03} = 6.806142443103933$ | $\alpha_{13} = -1.871324314462178$ | $\alpha_{23} = -0.9182009402333999$ |
| $\alpha_{04} = -3.85460683232795$ | $\alpha_{14} = 0.9868265691799668$ | $\alpha_{24} = 1.18865070517505$ |
| $\alpha_{05} = 1.24184273293118$ | $\alpha_{15} = -0.3113972943386534$ | $\alpha_{25} = -0.5421269487366867$ |
| $\alpha_{06} = -0.17364045548853$ | $\alpha_{16} = 0.0435662157231089$ | $\alpha_{26} = 0.09591004701167$ |
| $w_3 = 1.101388888888889$ | $w_4 = 0.98125$ | |
| $\alpha_{30} = -0.02059051845556993$ | $\alpha_{40} = -0.07348090746306993$ | |
| $\alpha_{31} = 0.1938604723378735$ | $\alpha_{41} = 0.4017323410950057$ | |
| $\alpha_{32} = -0.9307619464602723$ | $\alpha_{42} = -0.8172949898455654$ | |
| $\alpha_{33} = 0.3832374598448738$ | $\alpha_{43} = 0.3823215940101896$ | |
| $\alpha_{34} = 0.284794991077373$ | $\alpha_{44} = -0.6524848716111036$ | |
| $\alpha_{35} = 0.1783035348002281$ | $\alpha_{45} = 0.8535888895272106$ | |
| $\alpha_{36} = -0.10916135474896$ | $\alpha_{46} = -0.08856228536258634$ | |
| $\alpha_{37} = 0.0203173616044539$ | $\alpha_{47} = -0.005819770350080597$ | |

**Table A.8**
Scheme *E*8: optimized boundary coefficients for conservative 7th order first derivative approximation with 8th order interior scheme.

| | | |
|---|---|---|
| $w_0 = 0.3042245370370371$ | $w_1 = 1.460383597883598$ | $w_2 = 0.453463955026455$ |
| $\alpha_{00} = -3.241291470961598$ | $\alpha_{10} = 0.01177358173931513$ | $\alpha_{20} = 0.02137340875607741$ |
| $\alpha_{01} = 12.18747462483564$ | $\alpha_{11} = -2.687045796771664$ | $\alpha_{21} = -0.3138444129057621$ |
| $\alpha_{02} = -28.65616118692474$ | $\alpha_{12} = 7.329660288700824$ | $\alpha_{22} = -0.8515445548298325$ |
| $\alpha_{03} = 47.97898904051615$ | $\alpha_{13} = -11.15932057740165$ | $\alpha_{23} = 1.803089109659665$ |
| $\alpha_{04} = -54.14040296731185$ | $\alpha_{14} = 12.49081738841873$ | $\alpha_{24} = -1.003861387074581$ |
| $\alpha_{05} = 40.51232237384948$ | $\alpha_{15} = -9.409320577401648$ | $\alpha_{25} = 0.4697557763263318$ |
| $\alpha_{06} = -19.32282785359141$ | $\alpha_{16} = 4.529660288700824$ | $\alpha_{26} = -0.1515445548298325$ |
| $\alpha_{07} = 5.330331767692783$ | $\alpha_{17} = -1.260855320581188$ | $\alpha_{27} = 0.02901272995138073$ |
| $\alpha_{08} = -0.648434328104455$ | $\alpha_{18} = 0.154630724596458$ | $\alpha_{28} = -0.0024361150534464$ |
| $w_3 = 1.471428571428572$ | $w_4 = 0.7393931878306879$ | $w_5 = 1.082473544973545$ |
| $\alpha_{30} = -0.08629153295973042$ | $\alpha_{40} = 0.04666741189303745$ | $\alpha_{50} = 0.1545229278707249$ |
| $\alpha_{31} = 0.7141417874873672$ | $\alpha_{41} = -0.3828631046681091$ | $\alpha_{51} = -1.176309860878165$ |
| $\alpha_{32} = -2.749496256205785$ | $\alpha_{42} = 1.406687533005049$ | $\alpha_{52} = 3.838129674155415$ |
| $\alpha_{33} = 4.048992512411571$ | $\alpha_{43} = -3.213375066010097$ | $\alpha_{53} = -6.876824222306842$ |
| $\alpha_{34} = -4.373740640514463$ | $\alpha_{44} = 3.016718832512621$ | $\alpha_{54} = 6.86368547404324$ |
| $\alpha_{35} = 3.998992512411571$ | $\alpha_{45} = -1.613375066010097$ | $\alpha_{55} = -4.712134614626217$ |
| $\alpha_{36} = -2.082829589539119$ | $\alpha_{46} = 1.006687533005048$ | $\alpha_{56} = 1.973722503472796$ |
| $\alpha_{37} = 0.6069989303445101$ | $\alpha_{47} = -0.3066726284776329$ | $\alpha_{57} = 0.1402763154879514$ |
| $\alpha_{38} = -0.0767677234359209$ | $\alpha_{48} = 0.0395245547501803$ | $\alpha_{58} = -0.25779890216368$ |
| | | $\alpha_{59} = 0.0527307049447768$ |
| $w_6 = 0.9886326058201058$ | | |
| $\alpha_{60} = -0.1169355928394403$ | | |
| $\alpha_{61} = 0.8742458553587963$ | | |
| $\alpha_{62} = -2.780755136713333$ | | |
| $\alpha_{63} = 4.795937631999022$ | | |
| $\alpha_{64} = -4.557263616542921$ | | |
| $\alpha_{65} = 1.463970703555345$ | | |
| $\alpha_{66} = 0.152306568075446$ | | |
| $\alpha_{67} = 0.02309551624469717$ | | |
| $\alpha_{68} = 0.1718256962556173$ | | |
| $\alpha_{69} = -0.02281513218755944$ | | |
| $\alpha_{610} = -0.003612493205669607$ | | |

**Table A.9**
Scheme *T*4: optimized boundary coefficients for conservative 3rd order compact first derivative approximation with 4th order tridiagonal interior scheme.

| | | |
|---|---|---|
| $w_0 = -0.2282140125155382$ | $w_1 = 5.966147122794405$ | $w_2 = 1.798431523850588$ |
| $\beta_{0,1} = 17.82069083331248$ | $\beta_{1,-1} = 0.0990766937835805$ | $\beta_{2,-1} = 0.25$ |
| $\alpha_{00} = -7.77356361110416$ | $\beta_{1,1} = -0.2027699186492585$ | $\beta_{2,1} = 0.25$ |
| $\alpha_{01} = -5.910345416656241$ | $\alpha_{10} = -0.548768925044774$ | $\alpha_{21} = -0.75$ |
| $\alpha_{02} = 16.32069083331248$ | $\alpha_{12} = 0.75$ | $\alpha_{23} = 0.75$ |
| $\alpha_{03} = -2.63678180555208$ | $\alpha_{13} = -0.201231074955226$ | |

**Table A.10**
Scheme *T*6: optimized boundary coefficients for conservative 5th order compact first derivative approximation with 6th order tridiagonal interior scheme.

| | |
|---|---|
| $w_0 = -0.07171661720728502$ | $w_1 = 1.272166070449745$ |
| $\beta_{0,1} = 6.73683249485278$ | $\beta_{1,-1} = 0.4885251620537967$ |
| $\alpha_{00} = -3.630699832303889$ | $\beta_{1,1} = 2.7185849538713$ |
| $\alpha_{01} = -2.298235202757178$ | $\alpha_{10} = -1.179536538995937$ |
| $\alpha_{02} = 8.47366498970556$ | $\alpha_{12} = -1.34882079489275$ |
| $\alpha_{03} = -3.403499161519447$ | $\alpha_{13} = 3.347002160717289$ |
| $\alpha_{04} = 0.9956108316175933$ | $\alpha_{14} = -0.9569693577017375$ |
| $\alpha_{05} = -0.136841624742639$ | $\alpha_{15} = 0.138324530873136$ |
| $w_2 = -3.628896666385055$ | $w_3 = -2.532048718637736$ |
| $\beta_{2,-1} = -0.3891997445794$ | $\beta_{3,-1} = -0.5719411698333015$ |
| $\beta_{2,1} = -1.111732822492133$ | $\beta_{3,1} = -0.1193039182499841$ |
| $\alpha_{20} = 0.1648977096656178$ | $\alpha_{30} = -0.06789558773749761$ |
| $\alpha_{21} = -0.35630014899535$ | $\alpha_{31} = 0.5757385576666454$ |
| $\alpha_{23} = 1.018622137082022$ | $\alpha_{32} = -0.9286568616388836$ |
| $\alpha_{24} = -0.9355996594392$ | $\alpha_{34} = 0.5137393810208426$ |
| $\alpha_{25} = 0.10837996168691$ | $\alpha_{35} = -0.09292548931110686$ |

## Appendix B. Comparison schemes

In this work, the performance of the presently developed schemes are compared with others in the literature which have been labeled *S*1, *S*2, and *S*3. Details of the schemes may be found in Section 4. The coefficients of *S*1, *S*2, and *S*3 are given in Tables B.11,B.12, and B.13, respectively. In addition, *S*3 utilizes the unique interior discretization shown in Table B.14

**Table B.11**
Scheme $S1$: boundary coefficients for the explicit 5th order scheme from Ref. [1] coupled with the 6th order compact interior scheme.

| | |
|---|---|
| $\alpha_{00} = -2.589645595238095$ | $\alpha_{10} = -0.2019837698412698$ |
| $\alpha_{01} = 7.068066944444444$ | $\alpha_{11} = -1.073161111111111$ |
| $\alpha_{02} = -10.97584416666667$ | $\alpha_{12} = 1.980625833333334$ |
| $\alpha_{03} = 12.91247916666667$ | $\alpha_{13} = -0.9862805555555563$ |
| $\alpha_{04} = -10.44855138888889$ | $\alpha_{14} = 0.3381847222222228$ |
| $\alpha_{05} = 5.490774166666666$ | $\alpha_{15} = -0.0640533333333336$ |
| $\alpha_{06} = -1.6874725$ | $\alpha_{16} = 0.008398611111111173$ |
| $\alpha_{07} = 0.230193373015873$ | $\alpha_{17} = -0.00173039682539683$ |

**Table B.12**
Scheme $S2$: boundary coefficients for the compact 5th order scheme from Ref. [12].

| | |
|---|---|
| $\beta_{0,1} = 4$ | $\beta_{1,-1} = \frac{3}{14}$ |
| $\alpha_{00} = -\frac{37}{12}$ | $\beta_{1,1} = \frac{3}{14}$ |
| $\alpha_{01} = \frac{2}{3}$ | $\alpha_{10} = -\frac{19}{28}$ |
| $\alpha_{02} = 3$ | $\alpha_{11} = -\frac{5}{42}$ |
| $\alpha_{03} = -\frac{2}{3}$ | $\alpha_{12} = \frac{6}{7}$ |
| $\alpha_{04} = \frac{1}{12}$ | $\alpha_{13} = -\frac{1}{14}$ |
| | $\alpha_{14} = \frac{1}{84}$ |

**Table B.13**
Scheme $S3$: boundary coefficients for the compact 4th order scheme from Ref. [14].

| | | |
|---|---|---|
| $\beta_{0,1} = 9.2793108237360826$ | $\beta_{1,-1} = 0.11737546726594537$ | $\beta_{2,-2} = -0.067477420334188354$ |
| $\beta_{0,2} = 9.8711877434133051$ | $\beta_{1,1} = 0.92895849448052303$ | $\beta_{2,-1} = -0.1945509344676567$ |
| $\alpha_{00} = -3.6564773244914637$ | $\beta_{1,2} = -0.067839996199150834$ | $\beta_{2,1} = 1.279565347145571$ |
| $\alpha_{01} = -9.9196421679170452$ | $\alpha_{10} = -0.4197688256685424$ | $\beta_{2,2} = 0.20842348769505742$ |
| $\alpha_{02} = 10.088151775649886$ | $\alpha_{11} = -0.9740860609654658$ | $\alpha_{20} = 0.20875393530974462$ |
| $\alpha_{03} = 4.1769460418803268$ | $\alpha_{12} = 1.1593253854830003$ | $\alpha_{21} = -0.36722447739446801$ |
| $\alpha_{04} = -0.82222305192207212$ | $\alpha_{13} = 0.31685797023808876$ | $\alpha_{22} = -1.4711209307195428$ |
| $\alpha_{05} = 0.14757709267988142$ | $\alpha_{14} = -0.096453054902842381$ | $\alpha_{23} = 0.98917602108458036$ |
| $\alpha_{06} = -0.014332365879513103$ | $\alpha_{15} = 0.015579947274307879$ | $\alpha_{24} = 0.63518969715000262$ |
| | $\alpha_{16} = -0.0014553614585464077$ | $\alpha_{25} = 0.0042145635666246068$ |
| | | $\alpha_{26} = 0.0010111910030585999$ |

**Table B.14**
4th order interior discretization from ref. [20] used with boundary scheme $S3$.

| $\delta_1$ | $\delta_2$ | $\gamma_1$ | $\gamma_2$ | $\gamma_3$ |
|---|---|---|---|---|
| 0.5862704032801503 | 0.09549533555017055 | 0.6431406736919156 | 0.2586011023495066 | 0.007140953479797375 |

## Supplementary material

Supplementary material associated with this article can be found, in the online version, at doi:10.1016/j.compfluid.2018.12.010.

## References

[1] Carpenter MH, Gottlieb D, Abarbanel S. The stability of numerical boundary treatments for compact high-Order finite-Difference schemes. J Comput Phys 1993;108(2):272–95. doi:10.1006/jcph.1993.1182.

[2] Colonius T. Modelling artificial boundary conditions for compressible flow. Annu Rev Fluid Mech 2004;36:315–45. doi:10.1146/annurev.fluid.36.050802.121930.

[3] Cook AW, Dimotakis PE. Transition stages of RayleighTaylor instability between miscible fluids. J Fluid Mech 2001;457:69–99. doi:10.1017/S0022112002007802.

[4] Nagarajan S, Lele SK, Ferziger JH. A robust high-order compact method for large eddy simulation. J Comput Phys 2003;191(2):392–419. doi:10.1016/S0021-9991(03)00322-X.

[5] Cook AW. Artificial fluid properties for large-eddy simulation of compressible turbulent mixing. Phys Fluids 2007;19(5). doi:10.1063/1.2728937.

[6] Terashima H, Kawai S, Yamanishi N. High-Resolution numerical method for supercritical flows with large density variations. AIAA J 2011;49(12):2658–72. doi:10.2514/1.J051079.

[7] Ryu J, Livescu D. Turbulence structure behind the shock in canonical shock-vortical turbulence interaction. J Fluid Mech 2014;756:R1. doi:10.1017/jfm.2017.542.

[8] Tian Y, Jaberi F, Li Z, Livescu D. Numerical study of variable density turbulence interaction with a normal shock wave. J Fluid Mech 2017;829:551–88. doi:10.1017/jfm.2014.477.

[9] Gustafsson B. The convergence rate for difference aproximations to mixed initial boundary value problems. Math Comput 1975;29(130):396–406.

[10] Carpenter MH, Gottlieb D, Abarbanel S. Time-stable boundary conditions for finite-difference schemes solving hyperbolic systems: methodology and application to high-order compact schemes. J Comput Phys 1994;111:220–36. doi:10.1006/jcph.1994.1057.

[11] Hagstrom T, Hagstrom G. Grid stabilization of high-order one-sided differencing i: first-order hyperbolic systems. J Comput Phys 2007;223(1):316–40. doi:10.1016/j.jcp.2006.09.017.

[12] Cook AW, Riley JJ. Direct numerical simulation of a turbulent reactive plume on a parallel computer. J Comput Phys 1996;129(2):263–83. doi:10.1006/jcph.1996.0249.

[13] Visbal MR, Gaitonde DV. On the use of higher-order finite-difference schemes on curvilinear and deforming meshes. J Comput Phys 2002;181(1):155–85. doi:10.1006/jcph.2002.7117. http://www.sciencedirect.com/science/article/pii/S0021999102971172

[14] Turner JM, Haeri S, Kim JW. Improving the boundary efficiency of a compact finite difference scheme through optimising its composite template. Computers & Fluids 2016;138:9–25. doi:10.1016/j.compfluid.2016.08.007.

[15] Lele SK. Compact finite difference schemes with spectral-like resolution. J Comput Phys 1992;103(1):16–42. doi:10.1016/0021-9991(92)90324-R. http://www.sciencedirect.com/science/article/pii/002199919290324R

[16] Moin P. Fundamentals of engineering numerical analysis. Cambridge University Press; 2001.

[17] LeVeque RJ. Numerical methods for conservation laws. Springer; 1992.

[18] Perot JB. Discrete conservation properties of unstructured mesh schemes. Annu Rev Fluid Mech 2011;43(1):299–318. doi:10.1146/annurev-fluid-122109-160645.

[19] Anderson JD. Computational fluid dynamics: the basics with applications. Mc-Graw-Hill Series in Mechanical Engineering. McGraw-Hill; 1995.

[20] Kim JW. Optimised boundary compact finite difference schemes for computational aeroacoustics. J Comput Phys 2007;225(1):995–1019. doi:10.1016/j.jcp.2007.01.008.

[21] Strang G. Linear algebra and its applications. Thomson Brooks/Cole; 2006.

[22] Abarbanel SS, Chertock AE, Yefet A. Strict stability of high-Order compact implicit finite-Difference schemes: the role of boundary conditions for hyperbolic PDEs, II. J Comput Phys 2000;160(1):67–87. doi:10.1006/jcph.2000.6421.

[23] Yee HC, Sandham ND, Djomehri MJ. Low-dissipative high-order shock-capturing methods using characteristic-based filters. J Comput Phys 1999;150(May 1998):199–238.